OPINCHARGE

# OPINCHARGE
# D3.1 Isotope Based Studies Results - Description of the parameters and results from successful set ups developed for NMR, OEMS, neutron imaging and FIB-SIMS, isotope-based analyses

11/2025

Funded by the European Union

| | |
|---|---|
| **Lead Beneficiary** | Luxembourg Institute of Science and Technology |
| **Author(s)/Organisation(s)** | **S. Sharma (LIST)** |
| **Contact Email** | **sayantan.sharma@list.lu** |
| **Contributor(s)** | **X. L. Zhang (PSI), L. Skarjan (PSI), S. Trabesinger (PSI), S. Eswara (LIST)** |
| **Work Package** | Operando, in-situ, and ex-situ characterization of interfaces using isotopes |
| **Delivery Date (DoA)** | **30.11.2025** |
| **Actual Delivery Date** | **30.11.2025** |
| **Abstract:** | Studying interfaces, especially under operando conditions, remains one of the most challenging aspects of battery characterization. Nuclear Magnetic Resonance (NMR) spectroscopy, neutron imaging, Online Electrochemical Mass Spectrometry (OEMS), and Focused Ion Beam–Secondary Ion Mass Spectrometry (FIB-SIMS) imaging constitute a complementary set of isotope-sensitive techniques with the potential to provide profound insights into interfacial reactions and lithium dynamics in batteries. Although the fundamental principles of these methods are well established, further development is required to achieve seamless operando workflows with enhanced resolution and sensitivity.<br><br>This report summarizes the work carried out within the OPINCHARGE project to develop innovative operando methodologies using these techniques to investigate lithium-ion dynamics and associated degradation processes inside batteries during operation. It describes the design of specialized setups tailored to each operando method and highlights the insights gained into lithium-ion battery behavior through these approaches. |

| Document Revision History | | | |
|---|---|---|---|
| **Date** | **Version** | **Author/Contributor/Reviewer** | **Summary of Main Changes** |
| **30/11/2025** | 1.0 | S. Sharma et al. | Original version |

| Dissemination Level and Nature of the Deliverable | | |
|---|---|---|
| **PU** | Public | Yes |
| **SEN** | Sensitive, limited under the conditions of the Grant Agreement | No |
| **Nature** | R = Report, E = Ethics or, O = Other | R |



Funded by the European Union

| OPINCHARGE Consortium | | | |
|---|---|---|---|
| # | Participant Organisation Name | Short Name | Country |
| 1 | LUXEMBOURG INSTITUTE OF SCIENCE AND TECHNOLOGY (LIST) | LIST | LU |
| 2 | CENTRE NATIONAL DE LA RECHERCHE SCIENTIFIQUE CNRS (CNRS) | CNRS | FR |
| 3 | CENTRO DE INVESTIGACION COOPERATIVA DE ENERGIAS ALTERNATIVAS FUNDACION, CIC ENERGIGUNE FUNDAZIOA (CIC ENERGIGUNE) | CIC ENERGIGUNE | ES |
| 4 | DEUTSCHES ZENTRUM FUR LUFT - UND RAUMFAHRT EV (DLR) | DLR | DE |
| 5 | DEUTSCHES FORSCHUNGSZENTRUM FUR KUNSTLICHE INTELLIGENZ GMBH (DFKI) | DFKI | DE |
| 6 | FEI ELECTRON OPTICS BV (THERMO) | THERMO | NL |
| 7 | FUNDACION CIDETEC (CIDETEC) | CIDETEC | ES |
| 8 | FORSCHUNGSZENTRUM JÜLICH (FZJ) | FZJ | DE |
| 9 | PEDAL CONSULTING SRO (PEDAL) | PEDAL | SK |
| 10 | PAUL SCHERRER INSTITUT (PSI) | PSI | CH |

**NOTICE**

Funded by the European Union under grant agreement number 101104032 . Views and opinions expressed are however those of the author(s) only and do not necessarily reflect those of the European Union or European Climate, Infrastructure and Environment Executive Agency (CINEA). Neither the European Union nor the granting authority can be held responsible for them.

**OPINCHARGE**

Grant Agreement: 101104032 .

Call: HORIZON-CL5-2022-D2-01.

Topic: HORIZON-CL5-2022-D2-01-02.

Type of action: HORIZON Research and Innovation Actions.

Granting authority: European Climate, Infrastructure and Environment Executive Agency.

Grant managed through EU Funding & Tenders Portal: Yes (eGrants).

Project starting date: fixed date: 1 June 2023.

Project end date: 31 May 2026.

Project duration: 36 months.

## Table of Contents



## List of Tables



## List of Figures





Funded by the European Union

OPINCHARGE

Funded by the European Union

# 1.0 Introduction

Isotopes are nuclides of a given element that share the same atomic number (Z) but differ in mass number due to variations in the number of neutrons (N) within the nucleus. Since they contain an identical number of protons, isotopes exhibit nearly identical chemical properties. Isotopic analysis is essential across a wide range of scientific disciplines. In biology, isotopes are employed as tracers to study metabolic processes in plants, animals, humans, and microorganisms[1-5]. Archaeology makes use of isotopic techniques to date fossilized remains[6,7], in the physical sciences domain, isotopes serve as markers for investigating processes such as diffusion and corrosion[8]. Isotopic methods are also central to geochronology and geochemistry, where they are employed to analyze history and composition of planetary bodies[9-11]. Energy-storage materials research also benefits from isotopic studies as they contribute to advances in understanding charge transport and related bottlenecks[12,13].

**Li isotope tracing in batteries**

For Li two stable isotopes exist: ${}^{6}_{3}Li$ and ${}^{7}_{3}Li$. Both possess Z = 3, but their mass numbers differ by one unit, corresponding to the presence of an additional neutron in ${}^{7}_{3}Li$. The natural abundances of lithium isotopes are not identical. Among the two stable isotopes, $^{7}$Li is the more prevalent, comprising approximately 92.4% of naturally occurring lithium (hereafter referred to as $^{Nat}$Li), while $^{6}$Li accounts for about 7.6% of $^{Nat}$Li. There are commercially available lithium materials that exhibit isotopic compositions that deviate from natural abundance. These materials are enriched by a specific isotope. Such materials are termed as isotopically labeled. They have been extensively employed in battery

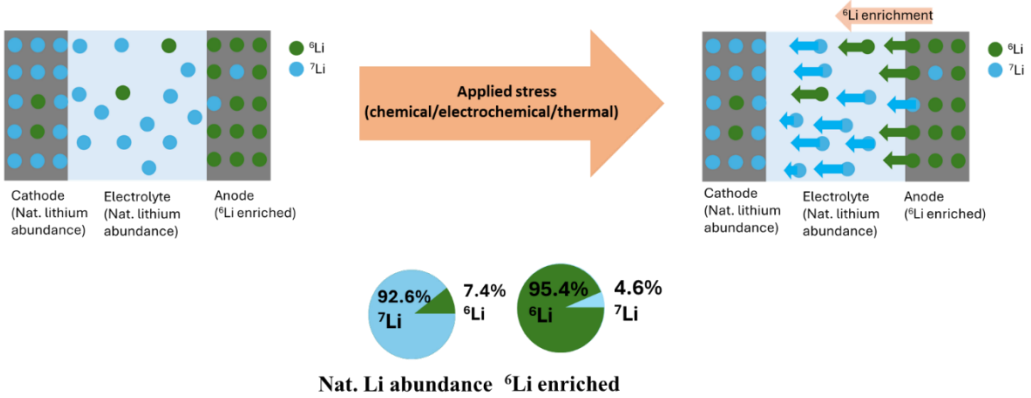


*Figure 1 Schematic describing isotope tracing process for a two-electrode cell with isotopically labelled (enriched in $^{6}$Li up to 95.4%) anode.*

research to elucidate Li transport mechanisms across different cell components[13-15]. As mentioned previously, $^{6}$Li and $^{7}$Li share identical chemical properties, so isotopically labeled materials as battery components enable the use of isotope-sensitive analytical techniques to track variations in isotopic abundance arising from directional flow of Li due to applied chemical, electrochemical or thermal stress. This is referred here to as isotope tracing (Figure 1).

The isotope tracing studies can be instrumental in deciphering the ion transport pathways in batteries, especially at the interfaces and through the passivating interfacial layers (SEI, CEI) via *operando* analysis. Here we report on the development of both ex-situ and operando analysis workflows for Li isotope tracing in batteries using different isotope sensitive techniques. The techniques described in this report are namely NMR, OEMS SIMS, and neutron imaging. Complementary information from



Funded by the European Union
OPINCHARGE

these techniques provides details about both the surface and bulk of the sample at different length scales, allowing analysis of the battery sample both at particle scale and electrode scale.

This report details the findings from conventional ex-situ analysis as well as innovative operando workflows developed within the framework of this project for accelerating isotope tracing studies in operando conditions.

# References:


1. Angelo M, Bendall SC, Finck R, et al. Multiplexed ion beam imaging of human breast tumors. Nat Med. 2014;20(4):436-442. doi:10.1038/nm.3488

2. Cabin-Flaman A, Monnier AF, Coffinier Y, et al. Combed Single DNA Molecules Imaged by Secondary Ion Mass Spectrometry. Anal Chem. 2011;83(18):6940-6947. doi:10.1021/ac201685t

3. Nelson CJ, Millar AH. Protein turnover in plant biology. Nat Plants. 2015;1(3):15017. doi:10.1038/nplants.2015.17

4. Steinhauser ML, Bailey AP, Senyo SE, et al. Multi-isotope imaging mass spectrometry quantifies stem cell division and metabolism. Nature. 2012;481(7382):516-519. doi:10.1038/nature10734

5. Ziesche RF, Kardjilov N, Kockelmann W, Brett DJL, Shearing PR. Neutron imaging of lithium batteries. Joule. 2022;6(1):35-52. doi:10.1016/j.joule.2021.12.007

6. Stolarski J, Meibom A, Przeniosło R, Mazur M. A Cretaceous Scleractinian Coral with a Calcitic Skeleton. Science (1979). 2007;318(5847):92-94. doi:10.1126/science.1149237

7. Wild EM, Teschler-Nicola M, Kutschera W, Steier P, Trinkaus E, Wanek W. Direct dating of Early Upper Palaeolithic human remains from Mladeč. Nature. 2005;435(7040):332-335. doi:10.1038/nature03585

8. De Souza RA, Martin M. Secondary ion mass spectrometry (SIMS) – a powerful tool for studying mass transport over various length scales. physica status solidi c. 2007;4(6):1785-1801. doi:10.1002/pssc.200675227

9. Misra S, Froelich PN. Lithium Isotope History of Cenozoic Seawater: Changes in Silicate Weathering and Reverse Weathering. Science (1979). 2012;335(6070):818-823. doi:10.1126/science.1214697

10. Wacey D, Kilburn MR, Saunders M, Cliff J, Brasier MD. Microfossils of sulphur-metabolizing cells in 3.4-billion-year-old rocks of Western Australia. Nat Geosci. 2011;4(10):698-702. doi:10.1038/ngeo1238

11. Yeung LY, Ash JL, Young ED. Biological signatures in clumped isotopes of O 2. Science (1979). 2015;348(6233):431-434. doi:10.1126/science.aaa6284

12. Berthault M, Buzlukov A, Dubois L, et al. Lithium isotope tracing in silicon-based electrodes using solid-state MAS NMR: a powerful comprehensive tool for the characterization of lithium batteries. Physical Chemistry Chemical Physics. 2023;25(33):22145-22154. doi:10.1039/d3cp02646a

13. Bofanova M, Delfino PM, Audinot JN, et al. Exploring Li pathways in Si-C/Gr electrodes and their SEI in Li batteries using Li isotope tracing by MAS NMR and FIB-SIMS. Nano Energy. 2025;144:111324. doi:10.1016/j.nanoen.2025.111324

14. Meyer T, Gutel T, Manzanarez H, Bardet M, De Vito E. Lithium Self-Diffusion in a Polymer Electrolyte for Solid-State Batteries: ToF-SIMS/ssNMR Correlative Characterization and Modeling Based on Lithium Isotopic Labeling. ACS Appl Mater Interfaces. 2023;15(37):44268-44279. doi:10.1021/acsami.3c08829

15. Meyer T, Gutel T, Manzanarez H, et al. Isotopic Labeling: A Powerful Tool to Investigate Lithium Transport in a Polymer-Ceramic Composite Electrolyte Designed for Solid-State Batteries. ACS Appl Energy Mater. Published online November 11, 2024. doi:10.1021/acsaem.4c02023

## 1.1 Operando, in-situ and ex-situ solid-state NMR studies of full cells including isotope labelled studies

Solid-state nuclear magnetic resonance (NMR) spectroscopy is particularly well suited for the investigation of battery materials- [[1],[2]]. Unlike diffraction-based techniques, it is a non-invasive and quantitative probe that does not rely on long-range structural order [[3],[4]], making it highly valuable for the study of disordered and heterogeneous phases such as those present in the solid–electrolyte interphase (SEI) [1,2]. In addition, solid-state NMR provides unique sensitivity to local environments and is exceptionally powerful for the detection and quantification of dynamic processes, including ion hopping and interfacial diffusion across distinct phases [[5],[6]]—for instance, between electrode bulk structures and the SEI [[7],[8],[9]].

Operando solid-state NMR spectroscopy has recently emerged as a powerful tool for probing electrochemical processes in batteries under realistic working conditions [2,[10],[11]]. Unlike ex situ or post-mortem analyses, operando NMR enables the direct observation of structural, compositional, and dynamic changes as they occur during cycling [10]. Because operando NMR experiments are generally conducted in static (non-MAS) mode—given the challenges of implementing fast magic-angle spinning in electrochemical cells—a combined analysis that integrates operando and ex situ approaches is highly valuable [[12]]. This strategy provides unique insight into local nuclear environments while also enabling the study of reaction intermediates, ion-transport pathways, and the evolution of interphases such as the SEI [9,10,[13]]. By coupling structural sensitivity with real-time monitoring of dynamics, solid-state NMR offers a complementary perspective to diffraction and other spectroscopic methods, advancing our understanding of degradation mechanisms and enabling the rational design of more stable electrode–electrolyte interphases [[14],[15]].

A particularly promising frontier is the integration of isotopic labelling into operando solid-state NMR [[16]]. The use of $^{6}$Li/$^{7}$Li, $^{13}$C or $^{2}$H-enriched species enhances sensitivity and enables the selective tracking of targeted components within complex electrochemical environments. For instance, $^{13}$C-enriched carbonate solvents can be employed to follow electrolyte degradation and SEI formation, while $^{6}$Li-enriched metal electrodes and electrolytes allow direct observation of isotope exchange processes at buried interfaces. Operando solid-state NMR, combined with ex situ NMR and isotopic labelling, not only improves signal-to-noise but can also provide mechanistic insight into reaction pathways, transport, and interphase evolution that would otherwise remain inaccessible. This combination offers a powerful route to probe electrochemical transformations.

As part of the OPINCHARGE project, we carried out a solid-state NMR study that integrates isotope-labelling schemes directly into operando and ex situ experiments. We tracked isotope exchange



Funded by the European Union

among cell components in half-cells employing LFP and Si/graphite electrodes, using $^{6}$Li metal anodes and, in separate experiments, $^{13}$C- and $^{2}$H-labelled organic electrolytes.

## 1.1.1 Operando and Ex Situ NMR of Lithiation, Li-Ion Transport, and SEI

Operando solid-state NMR allows real-time analysis of materials under operational conditions but operates in static mode, which limits resolution, especially for broad signals or complex interfaces like the SEI. The absence of magic angle spinning (MAS) further hinders detailed structural insights.

To address these limitations, combining ex situ and in situ NMR is essential. Ex situ NMR improves precise structural characterization, while in situ NMR captures real-time processes. This combined approach allows for a comprehensive analysis of material behavior in both operational and ideal conditions. In the following sections, the *ex situ* and operando NMR studies of Si/Gr composites and LFP electrodes are presented.

### 1.1.1.1 SEI in Si/graphite Electrodes (ex situ NMR)

The main goal of this part of the work is to characterize the organic and inorganic phases in the SEI, as well as Li exchange, using ex-situ solid-state NMR.

The systems investigated comprise Si/graphite (Si/Gr) electrode materials in a half-cell configuration. To probe SEI formation and its influence on the chemical and electrochemical characteristics, two electrolyte formulations were selected:

1. **EC-based**: 1.0 M $LiPF_6$ in EC:EMC (3:7 by wt.)
2. **FEC-based**: 1.0 M $LiPF_6$ in FEC:EMC (3:7 by wt.) + 2 wt.% VC.

This selection focuses on electrolytes that favor either LiF-rich (inorganic) or polymeric organic SEI formation. Fluoroethylene carbonate FEC, is known for preferential decomposition on the electrode surface during its initial cycles, promoting LiF-rich SEI layers.

While *in-situ* characterization provides a more realistic view of battery behavior, it does not allow for Magic Angle Spinning (MAS), which limits resolution in solid-state NMR experiments. Operando measurements are typically hindered by the inability to rotate cells rapidly.

Two *ex-situ* samples were prepared after the first discharge (lithiation) using EC- and FEC-based electrolytes. The resulting $^{7}$Li NMR spectra (Figure 1b) reveal three main signals at ~42, 10, and 0 ppm, corresponding to lithiated graphite, $Li_xSi$ phases (from Si lithiation), and diamagnetic $Li^+$ ions in the SEI, respectively.



Funded by the European Union

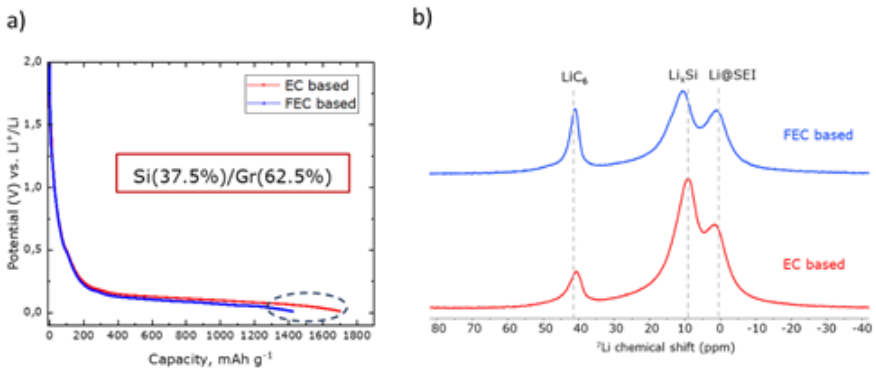


Figure 1. (a) Voltage profile of the first lithiation of the cells used for the *ex-situ* samples. (b) $^{7}$Li NMR spectra of the FEC- and EC-based samples, showing the presence of Li in the SEI, LixSi phases, and lithiated graphite ($LiC_6$).

To detect and confirm the presence of LiF in the SEI formed on both electrodes, $^{19}$F NMR experiments were conducted, and the resulting spectra are shown in Figure 2. A signal at ~-70 ppm is observed in both samples, corresponding to residual $PF_6^-$ molecules embedded in the SEI. Additionally, small resonances at ~-80 and -150 ppm are assigned to $PO_2F_2^-$ and $PO_3F_2^-$, respectively, resulting from the partial hydrolysis of $PF_6^-$.

The key difference between the spectra is a prominent signal at -204 ppm in the FEC-based sample, which is attributed to LiF. This confirms the formation of a LiF-rich inorganic SEI layer in the FEC-based material, consistent with FEC decomposition during SEI formation.

To further analyze the SEI composition, $^{1}$H NMR experiments were performed on solid samples. These results revealed a significantly higher concentration of proton-rich organic (polymeric) material in the sample cycled with the EC-based electrolyte.

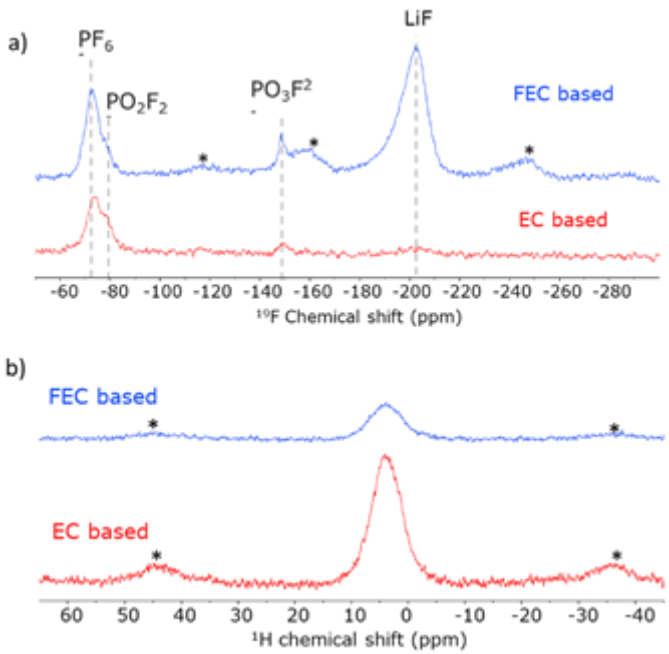


Figure 2. (a) $^{19}$F solid-state NMR spectra of FEC- and EC-based samples, showing the presence of LiF in the FEC sample and its absence in the EC sample. (b) $^{1}$H solid-state NMR spectra of FEC- and EC-based samples, indicating a higher concentration of organic material in the SEI of the EC-based sample.



Funded by the European Union

2D Exchange Spectroscopy (EXSY) in the solid state is an NMR technique used to investigate the reversible exchange of $Li^+$ ions between different lithium sites in equilibrium. In these homonuclear experiments, off-diagonal correlation signals between two sites at a given mixing time indicate $Li^+$ ions exchanging positions between sites with different chemical shifts.

A 2D EXSY experiment was performed for the FEC- and EC-based samples, as characterized by the $^7Li$ spectra in Figure 1b. The resulting 2D spectrum for the FEC sample, shown in Figure 3a ($^7Li$-$^7Li$ correlation), reveals no off-diagonal signals for the $LiC_6$ resonance. However, clear correlation signals are observed between the $^7Li$ SEI signal (0 ppm) and the LixSi resonance (~10 ppm) at a mixing time of 100 ms.

This result demonstrates, for the first time, the presence of $Li^+$ exchange between Si particles and the SEI. This finding is highly significant, as $Li^+$ exchange is directly linked to Li diffusion through the SEI and electrode accessibility—key parameters for SEI performance.

The 2D EXSY experiment proves to be a powerful tool for correlating SEI chemistry with its functional performance. It enables a direct comparison between LiF-rich and organic-rich SEI layers, which is a central goal of this study.

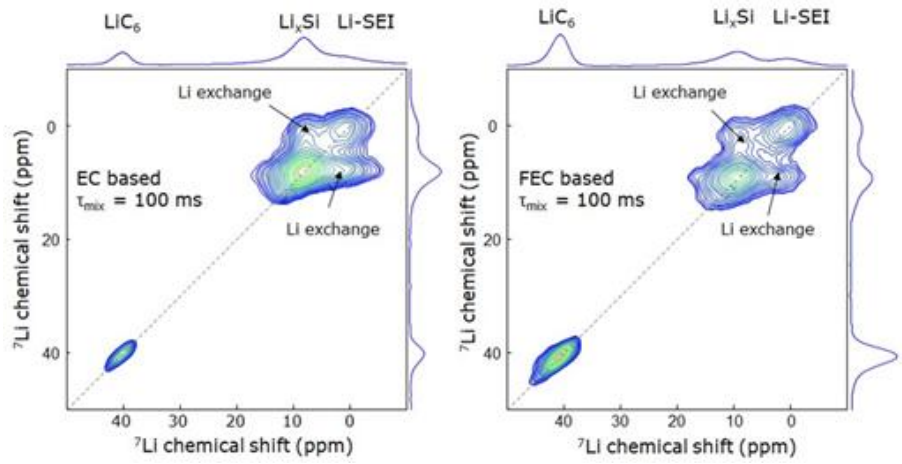


Figure 3. $^7Li$–$^7Li$ 2D EXSY experiments on ex situ Si/Gr samples obtained with EC-based (left) and FEC-based (right) electrolytes. In both cases, clear exchange cross-peaks are observed between Li in the SEI and Li in the Si particles, whereas no clear exchange signals are detected involving Li at the lithiated graphite sites ($LiC_6$).

Solid-state NMR cross-polarization (CP) experiments are effective for detecting heteronuclear spin species at close distances. For example, $^1H$-$^7Li$ experiments detect $Li^+$ ions near protons (polymeric SEI), while $^{19}F$-$^7Li$ correlations reveal LiF and Li-F spin interactions. Coupling CP to EXSY in CP-EXSY experiments allows assessing $Li^+$ exchange between distinct SEI components and Si particles at different mixing times.

Figure 4 shows $^7Li$ {$^1H$}-$^7Li$ CP-EXSY and $^7Li$ {$^{19}F$}-$^7Li$ CP-EXSY spectra for the FEC and EC samples. The main CP signals arise from dipolar-based magnetization transfer, while signal buildup (~10 ppm) at increasing EXSY mixing times corresponds to $Li^+$ exchange from the polymeric (organic) phase (in $^7Li$ {$^1H$}-$^7Li$ CP-EXSY) and LiF (in $^7Li$ {$^{19}F$}-$^7Li$ CP-EXSY) into Si particles.

A larger $Li^+$ exchange amplitude is observed from the organic phase compared to the inorganic LiF in FEC (Figures 4a and b). Similarly, $^7Li$ {$^1H$}-$^7Li$ CP-EXSY for the EC sample (Figure 4c) shows intense $Li^+$ exchange.

The $Li^+$ buildup intensities (Figure 4d) were fitted with single-exponential functions, yielding different exchange rates: EC: $\tau_{ex}$(SEI-$Li_xSi$) = 55 ms, $K_{ex}$ = 18 $s^{-1}$ FEC: $\tau_{ex}$(SEI-$Li_xSi$) = 40 ms, $K_{ex}$ = 25 $s^{-1}$



Funded by the European Union

The $^{7}Li\{^{1}H\}$-$^{7}Li$ CP-EXSY data show a larger $Li^{+}$ exchange amplitude for the EC sample, consistent with a more extensive organic SEI coating on Si particles than in the FEC sample. By contrast, the FEC sample exhibits faster $Li^{+}$ exchange, indicating higher $Li^{+}$ diffusivity through its SEI and cohering with its superior electrochemical performance [[17]]. This behavior can be rationalized by the LiF-rich SEI formed with FEC, which suppresses complete organic coverage at the Si surface and shifts a greater fraction of organic material farther from the Si particles. The CP-EXSY experiments provide valuable insights into the SEI structure and function, highlighting that the Li diffusivity and SEI composition critically influence performance. The faster exchange rate in the FEC-based SEI correlates with enhanced Li transport, a key parameter for SEI efficiency.

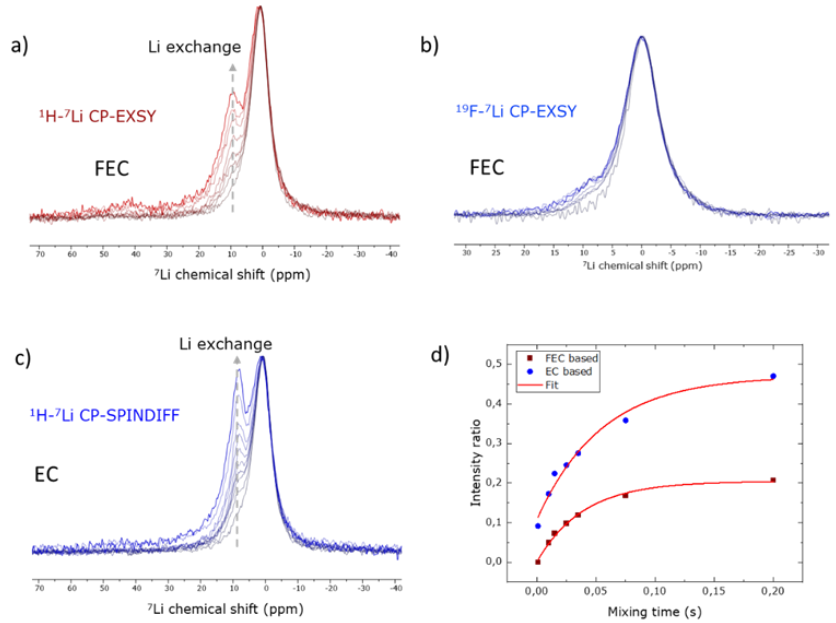


Figure 4. (a) $^{1}H$-$^{7}Li$ CP-EXSY experiments for FEC, (b) $^{19}F$-$^{7}Li$ CP-EXSY experiment for FEC, and (c) $^{1}H$-$^{7}Li$ CP-EXSY for EC. (d) $^{7}Li$ buildup signals from the $^{1}H$-$^{7}Li$ CP-EXSY experiments at increasing mixing times, fitted with single-exponential functions.

## 1.1.1.2 Si/graphite and Li Metal (operando NMR)

Solid-state cells for operando NMR studies were assembled using rectangular-shaped electrodes within a PEEK polymeric cage. The setup included a Si/Gr electrode, a Li metal counter-electrode, and an FEC-based electrolyte (1.0 M $LiPF_6$ in FEC:EMC (3:7, wt.) + 2 wt.% VC).

The in situ $^{7}Li$ NMR spectral evolution (Figure 5) shows the appearance of a broad signal between 10 and 40 ppm at each full discharge, corresponding to a superposition of resonances from lithiated $Li_xSi$ (~10 ppm) and $LiC_6$ (~40 ppm). As the *operando* NMR experiments were recorded in static cells, the resonances appear broadened compared to the *ex-situ* spectra in Figure 1, which were recorded under 20 kHz Magic Angle Spinning (MAS).

Additionally, a strong signal at 0 ppm, attributed to $Li^{+}$ ions in the electrolyte, decreases in intensity upon cycling. This reduction aligns with the partial precipitation of $Li^{+}$ ions from the liquid electrolyte into the solid SEI, though the SEI is not directly visible in the static spectra.

Oscillations in the $^{7}Li$ signal intensity are also observed for the Li-metal region (around 260 ppm). While no significant spectral changes are seen initially, an increase in signal intensity is noted after the first charge. Importantly, NMR signals from metals are not proportional to the bulk Li content but rather to the accessible surface, because the RF penetration is limited by the skin depth at the metal surface [[18],[19]]. The observed


Funded by the European Union
OPINCHARGE

increase therefore indicates the in-situ formation of a rougher Li surface (e.g., dendrites or disordered deposits) after the first and second charge.

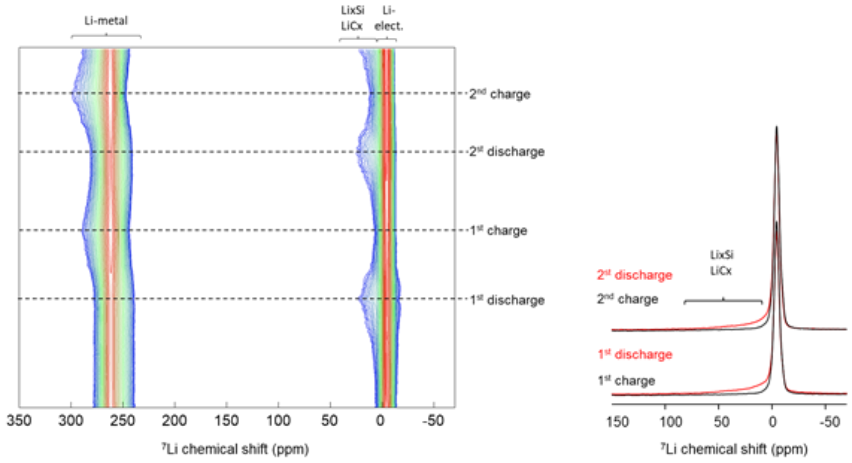


Figure 5. *Operando solid-state NMR was performed on a half-cell comprising a Si/Gr working electrode, a Li-metal counter electrode ($^7$Li), and an FEC-based electrolyte (1.0 M $LiPF_6$ in FEC:EMC, 3:7 wt/wt, with 2 wt% VC). The evolution of the $^7$Li NMR signal was monitored during electrochemical cycling. One-dimensional spectra were extracted from the 2D map at the indicated charge/discharge points (right panel). Spectral regions assigned to Li metal (240–280 ppm), lithiated graphite and silicon ($LiC_x$ and $Li_xSi$, ~5–50 ppm), and Li species in the SEI (~0 ± 10 ppm) are highlighted. No resolvable separation of the lithiated active-material signals is obtained under static (non-MAS) conditions.*

## 1.1.2 Operando and Ex Situ NMR with Isotope-Enriched Components

To track the evolution of materials and the SEI over time, isotopic labeling was introduced into both operando and ex situ characterizations

### 1.1.2.1 $^6$Li/$^7$Li Isotope Tracing in Operando NMR of Si/Gr–Li Metal Cells

To track Li-ion evolution in a Si/Gr half-cell, we conducted *in situ* measurements replacing the Li metal with $^6$Li-enriched material while using an EC-based electrolyte at natural $^7$Li abundance. The resulting $^7$Li NMR evolution is shown in Figure 6A. Both the Li-metal signal and the 10–50 ppm region—associated with $LiC_x$ and $Li_xSi$—follow the expected charge/discharge trends. Accordingly, at the dashed markers indicating fully discharged states in Figure 6B, the Li-metal signal reaches a maximum and the lithiated-Si/graphite signals a minimum; the corresponding Li-metal intensities at charge/discharge points are summarized in Figure 6C. Interestingly, an increase in the $^7$Li metal signal


Funded by the European Union
OPINCHARGE

is already visible during the first discharge—when $^{7}$Li plating is not yet expected—supporting our (and WP3 partners') conclusion that spontaneous isotope exchange occurs upon electrolyte–metal contact.

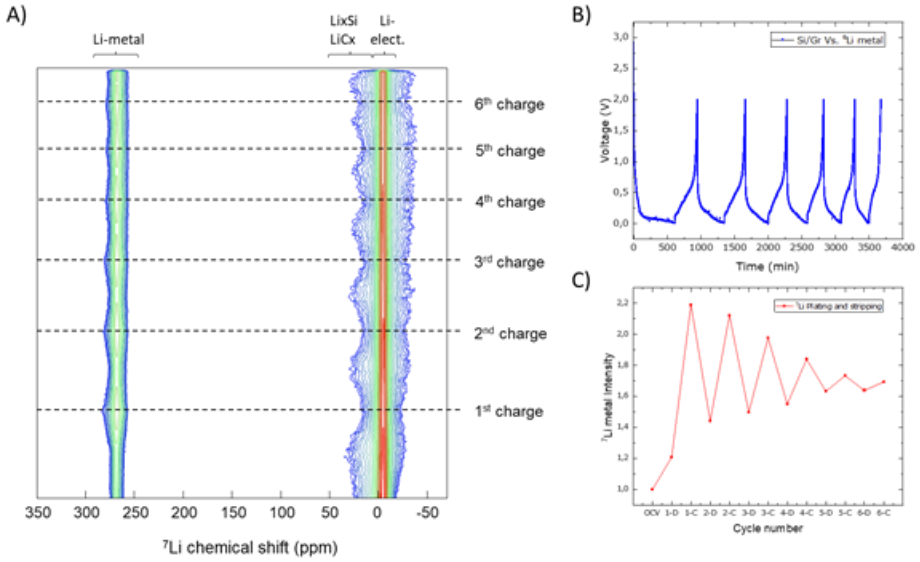


Figure 6. (A) Operando $^{7}$Li NMR of a half-cell with $^{6}$Li metal and an EC-based electrolyte (natural $^{7}$Li abundance). (B) Corresponding electrochemical profile. The $^{7}$Li metal resonance evolves markedly, consistent with $^{6}$Li↔$^{7}$Li isotopic exchange and redistribution during cycling.

Figure 6C compiles the evolution of the $^{7}$Li metal signal (from Figure 6A) at the indicated charge/discharge states. The oscillation amplitude decays with successive cycles, consistent with isotopic redistribution and progressive averaging of the $^{6}$Li/$^{7}$Li composition.

## 1.1.2.2 $^{2}$H Isotope Tracing in Operando and Ex Situ NMR of Si/Gr–Li Metal Cells

In Section 1.2.1 (SEI components and Li dynamics in EC- and FEC-based systems, ex situ), we found that the SEI formed with these electrolytes contains a high fraction of organic solid species and exhibits measurable Li dynamics across the layer. In this part of the work, d4-EC-labeled material was integrated into the same electrolyte configuration, and the evolution of this material was monitored operando and further characterized *ex situ*. EC was selected for this study as it will generate an organic-rich SEI that is better sutured for $^{13}$C and $^{2}$H characterizations.

An operando cell was prepared composed of a $^{7}$Li metal counter-electrode, a Si/Gr composite electrode, and an electrolyte, where EC was substituted by d4-EC. The aim of this experiment was to monitor the $^{2}$H NMR signal operando in order to evaluate the possible consumption of this molecule from the electrolyte to form a solid SEI in situ. The result is shown in Figure 6, where the deuterium signal was monitored during electrochemical cycling. The first relevant information from this cell is the rapid decrease of the $^{2}$H NMR signal during the first discharge process. This signal decay is followed by a slightly oscillating signal whose intensity remains approximately constant during the subsequent cycles. Therefore, this initial decay is assigned to the formation of a solid organic deposit containing


Funded by the European Union
OPINCHARGE

most of the $^{2}H$ NMR signal, which is eliminated from the spectrum. The formation of organic material from the initial d4-EC in solution is observed as an eliminated signal, where the deuterium from the solid compound is not detected due to quadrupolar broadening of the $^{2}H$ NMR in the solid state, longer relaxation times in solid compounds, and the heterogeneity of the solid. All these factors create a situation where the solid deuterated material cannot be easily identified in operando studies but will be further analyzed ex situ using MAS techniques in the following subsection.

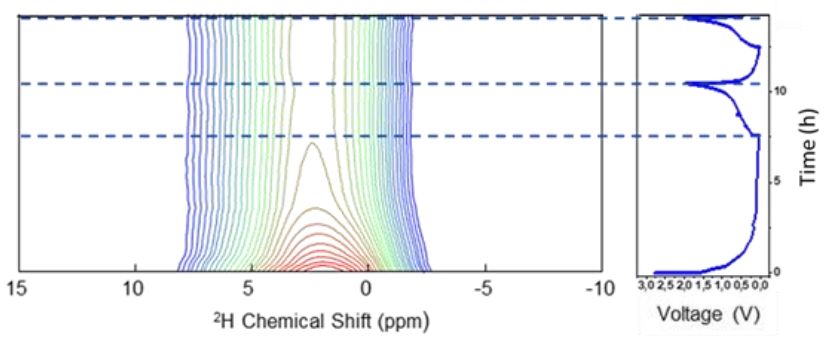


Figure 6: $^{2}H$ operando soldi state NMR evolution of the d4-EC signal upon electrochemical cycling

In addition to the first decay of the deuterium signal during the initial discharge, a slight oscillation of the signal is observed that clearly matches the electrochemical curves, as highlighted by the dashed lines in Figure 6. These oscillations were assigned to the minor reversible formation of the SEI and/or the reversible effects of ionic diffusion within the bulk of the electrolyte induced by the varying voltages.

To the best of our knowledge, this is the first time that $^{2}H$ NMR detection has been performed in a cell during an operando experiment.

In order to characterize the organic solid deposit of the SEI formed during the first discharge in a Si/Gr half-cell, two ex situ coin cells were discharged to 10 mV, and the electrodes were collected and packed into a rotor for MAS measurements. The electrochemical curves and the resulting $^{7}Li$ NMR spectrum are shown in Figure 7.

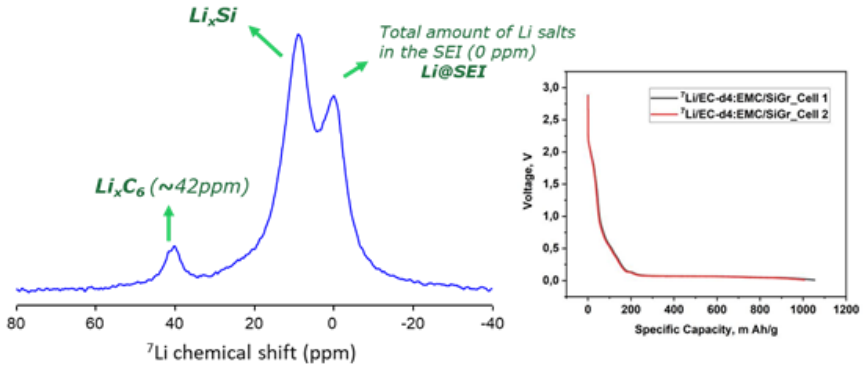


Figure 7: $^{7}Li$ NMR spectrum of the *ex situ* sample obtained by collecting the two electrodes “cell1” and “cell 2” after the first discharge



Funded by the European Union
OPINCHARGE

Three main signals are observed in the $^{7}$Li NMR spectrum of Figure 7, which are assigned to lithiated graphite ($Li_xC_6$), lithiated Si ($Li_xSi$), and Li at the SEI (Li@SEI). This spectrum is very similar to that obtained from the unlabeled material, as shown in Figure 1C.

$^{2}$H solid-state NMR measurements performed on the sample obtained after mixing both electrodes *ex situ* from the cells used in Figure 7 are shown in Figure 8.

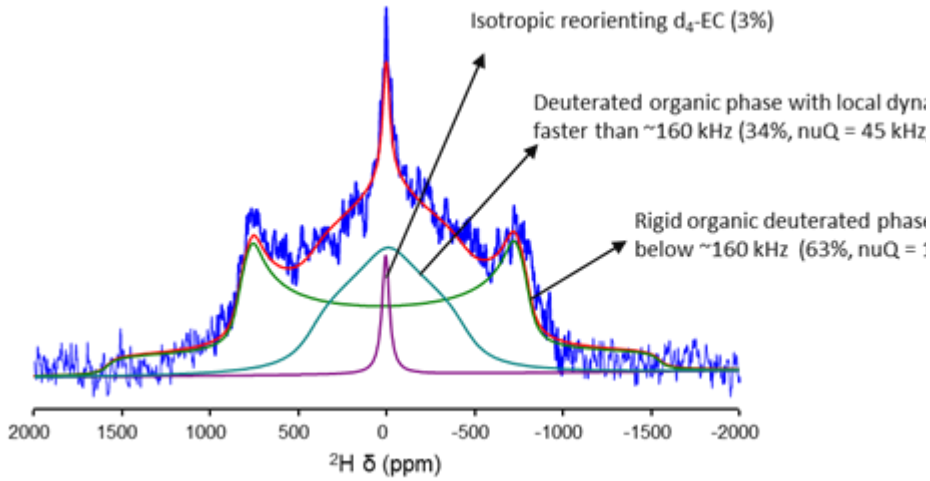


Figure 8. Ex situ $^{2}$H solid-state NMR spectrum obtained from a static measurement of the electrodes collected from the cells shown in Figure 7 after the first discharge.

The $^{2}$H solid-state NMR spectrum shown in Figure 8 presents three distinct components with different values of intensity, quadrupolar coupling, and asymmetry. In general, $^{2}$H spectra in the solid state are characterized by Pake-shaped patterns resulting from the quadrupolar interaction present for this isotope with nuclear spin I = 1 [[20]]. For rigid organic samples with fixed C–D bonds that are not subject to fast reorientations, the quadrupolar splittings are typically around ~160 kHz with no asymmetry [[21]]. This is, in fact, the main signal observed in the spectrum, accounting for approximately 63% of the total $^{2}$H NMR intensity.

Lower values of quadrupolar coupling are observed when local reorientations of the corresponding C–D bonds occur faster than the intrinsic quadrupolar coupling (160kHz in this case). This is the case for the intermediate signal, which accounts for approximately 34% of the organic phase. Finally, the low-intensity central Lorentzian line corresponds to liquid-like behavior, presumably arising from unreacted d4-EC in the SEI.

In general, $^{2}$H solid-state NMR is not able to resolve different chemical species, but it is a highly sensitive technique for assessing local dynamics and, in this case, for evaluating the rigidity of the SEI, which is a relevant parameter for understanding its performance.

## 1.1.2.3 $^{13}$C Isotope Tracing in Operando and Ex Situ NMR of Si/Gr–Li Metal Cells



Funded by the European Union

An in situ (operando) half-cell was prepared, consisting of a Si/Gr electrode, standard Li metal counter-electrode, and an electrolyte in which EC was homogeneously enriched with $^{13}C$ isotopes. $^{13}C$ NMR spectra were recorded as a function of electrochemical cycling. The results of this experiment are shown in Figure 9. Two main signals are observed during the experiment, corresponding to the two $^{13}C$ sites of EC: the two equivalent $CH_2$ carbons (~65 ppm) and the carbonate carbonyl C=O (~155 ppm), as expected. The evolution of the intensities of each of these resonances is shown in purple and green in the figure.

In line with observations made for $^{2}H$ operando experiments, the main finding is a reduction of the signals corresponding to the EC-labeled isotopes, which is more significant during the first discharge. This is consistent with SEI formation during the initial discharge process (Si/Gr lithiation). In addition, minor oscillations of the intensity were observed, which are coupled to the electrochemical cycling and assigned to variations in the bulk magnetic susceptibility of the electrodes, with a minor impact on the shifts and line broadening of the electrolyte signals.

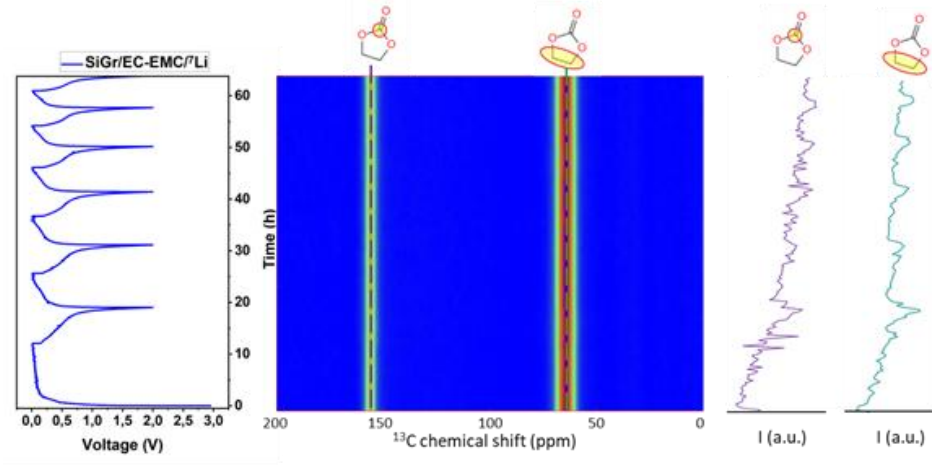


Figure 9: $^{13}C$ in-situ (operando) evolution of a half-cell composed of Si/Gr anode, Li metal with natural isotopic distribution, and an EC-based electrolyte with EC homogenously enriched in $^{13}C$ isotopes. The electrochemical evolution and the intensity of the $^{13}C$ signal evolution are shown in the figure.

Careful inspection of the 1D spectra associated with the electrochemical evolution in Figure 9 reveals an additional resonance between 10 and 50 ppm. Although faint in the 2D map, it is evident in the individual 1D traces. This feature, which does not match the $^{13}C$ resonance of EC, grows during the first cycle (Figure 10), consistent with the formation of an SEI degradation product. Its chemical shift is compatible with a $CH_2/CH_3$ carbon from an open-ring EC derivative (e.g., LEC or LBDC), as detailed in the *ex situ* characterization in the next chapter.



Funded by the European Union

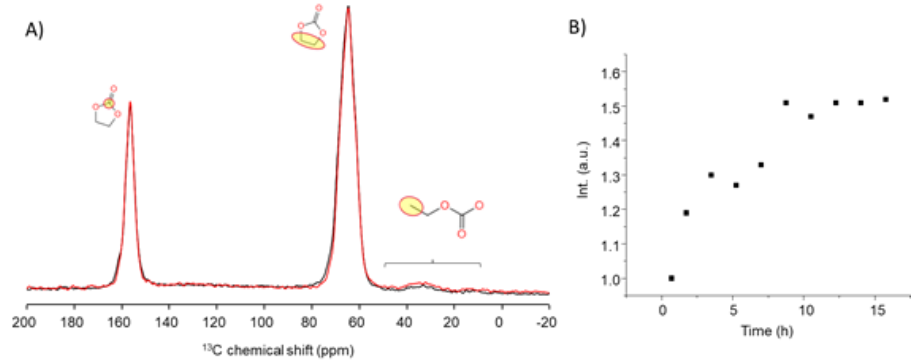


Figure 10. (A) 1D spectra extracted from the *in situ* 2D map in Figure 9 at time 0 (black) and after 15 h (red), i.e., upon completion of the first electrochemical cycle. The principal resonances correspond to the EC $^{13}$C sites (labels shown). A weak, broad feature appears near 30 ppm. (B) The intensity of this feature grows over the first cycle.

It should be noted that, because the in situ measurements are performed under static conditions, only signals from relatively mobile species are clearly observed; more rigid molecules—such as carbonates that may be present—are not easily detected in situ. The signals in the 10–50 ppm region observed in Figure 10 are therefore attributed to species undergoing relatively fast local reorientation, consistent with the proposed assignment.

As the $^{13}$C signal evolution obtained under operando conditions does not allow high-resolution detection of the solid components formed (due to the absence of magic-angle spinning), ex situ measurements were performed in parallel to obtain higher-resolution spectra under MAS conditions. The sample was prepared by packing into an NMR rotor the material obtained after extraction of the Si/Gr electrode from a coin cells stopped at the discharge.

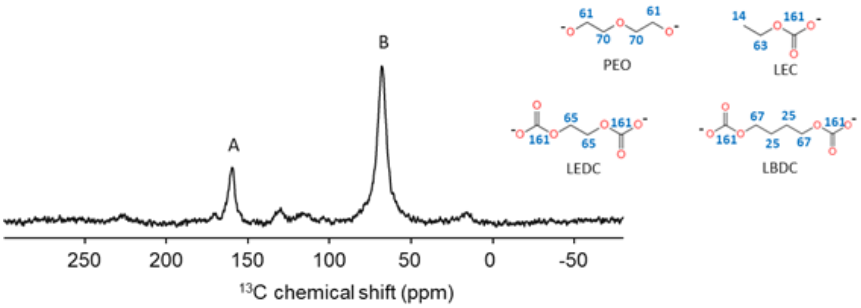


Figure 11: The ex situ $^{13}$C solid-state NMR spectrum of an electrode sample recovered from a cell comprising a $^{13}$C-labeled EC electrolyte, a Si/Gr composite, and a lithium-metal anode is shown. The structures of the possible compounds formed in the SEI from EC degradation as proposed previously are presented in the figure inset, together with the expected $^{13}$C NMR chemical shifts for the different carbon sites.

Two main $^{13}$C signals are observed, centred at ~70 and ~160 ppm (labelled B and A, respectively, in the figure). Owing to the intrinsic broadening of solid-state $^{13}$C NMR—further exacerbated by material heterogeneity—these resonances are not straightforward to assign. In principle, they could include contributions from residual, unreacted EC solvent embedded in the SEI. Nevertheless, we do not


Funded by the European Union
OPINCHARGE

consider EC a major constituent of the organic phase: the $^{2}H$ spectra of the ex situ sample prepared with $^{2}H$-labelled EC (Figure 8) indicate pronounced rigidity. Residual EC would be expected to exhibit relatively fast dynamics, whereas the $^{2}H$ data reveal that the dominant organic component is rigid. Previous *ex situ* solid-state NMR characterizations using homogeneously $^{13}C$-enriched EC resulted in a similar spectrum, with main resonances at ~160 and ~70 ppm. Based on those *ex situ* NMR results, the EC decomposition reactions shown in the figure inset were proposed—particularly PEO, LEC, LEDC, and LBDC [[22]]. The predicted $^{13}C$ chemical shifts for these molecules (highlighted in blue) place carbonyl carbons in the 161 ppm range, overlapping under signal A, and their alkyl/ethylene carbons in the 61–70 ppm region, consistent with the broad resonance B. Additionally, a minor resonance at ~170 ppm is attributable to lithium carbonate ($Li_2CO_3$), while a feature near ~133 ppm matches the expected $^{13}C$ response of lithiated graphite [[23]].

Consistent with the *in situ* evolution described above, an additional resonance appears within 10–50 ppm; here it occurs at a lower shift (~18 ppm, Figure 11). This feature is compatible with open-ring EC derivatives (LEC/LBDC) formed as degradation products. The absence of the ~30 ppm signal likely reflects material loss during the rinsing step used to prepare the *ex situ* sample.

### 1.1.2.4 $^{6}Li/^{7}Li$ Isotope Tracing in Operando NMR of LFP–Li Metal Cells

Operando NMR experiments were conducted in a cell composed of a Si/Gr composite electrode, the EC-based electrolyte described before, and a Li metal counter-electrode isotopically labeled with $^{6}Li$. The cell was cycled (Figure 12 A), and the NMR spectra were recorded during electrochemical cycling (Figure 12 B). Different signal evolutions are observed at various chemical shifts, as assigned in Figures 12 C and D, corresponding to bulk and dendritic Li metal, Li in the electrolyte at approximately 0 ppm, and Li in LFP, extracted as the intensity evolution around 60 ppm. Although the chemical shift for Li in LFP appears as a very broad resonance centered around 0 ppm due to paramagnetic interactions, this signal is so broad that under the static conditions used for recording this operando experiment, it is almost indistinguishable from the baseline in a single spectrum. Nevertheless, this broad component evolves as expected for Li in LFP, as will be discussed in the following section.

The cycling of this cell begins with a charging process up to approximately 3.8 V (Figure 12). During this time, a decrease in the $^{7}Li$ signal intensity at LFP is observed, as expected, because Li ions are extracted from the cathode and migrate to the Li metal through the electrolyte. Interestingly, the $^{7}Li$ signal intensity of lithium in the electrolyte increases during this period (blue line). This effect indicates that a spontaneous exchange occurred between $^{6}Li$ at the metal and the Li with natural isotope distribution in the electrolyte. This spontaneous exchange was also observed by other partners in WP3 and confirmed by us through liquid NMR measurements. As a consequence, with all Li migrated from the cathode to the electrolyte, a net increase in the $^{7}Li$ signal intensity is observed. Concurrently, both signals of Li metal centered at 263 and 280 ppm increase in $^{7}Li$ magnetization, as expected due to the plating of $^{7}Li$ metal at the surface of the Li electrode. After reaching 3.8 V, during the discharge, the reverse process is observed, where the $^{7}Li$ magnetization in the electrolyte and Li metal decreases as ions migrate back to the LFP cathode. During the second charge process and subsequent cycles, a cyclic behavior is observed, where the intensity of dendritic Li metal increases during charging and


Funded by the European Union
OPINCHARGE

decreases during discharging, coupled with the corresponding oscillations of the $^{7}$Li signal inside the LFP.

Interestingly, the signal evolution around 0 ppm, corresponding to $^{7}$Li ions in the electrolyte, appears to oscillate in chemical shift, with these oscillations matching the charge and discharge processes. We assign these oscillations and the observed changes in Li signal height to variations in the bulk magnetic susceptibility that occur when the Fe oxidation state changes between 2+ (lithiated state) and 3+ (delithiated state). Such variations in bulk magnetic susceptibility can slightly affect the chemical shifts of electrolyte signals in the vicinity, as they are in fast exchange during the course of the experiment.

It is also interesting to observe that the deposition of $^{7}$Li metal after the first cycle is seen as oscillations of the dendritic lithium at 280 ppm, and not at the surface of the bulk Li metal at 263 ppm, which is only clearly observed during the first cycle. We assign this observation to the preferential plating of lithium on top of microstructured Li particles, which act as seeds for further lithium growth, with limited access to the surface of the Li metal bulk.

Finally, it is noteworthy that, apparently, the overall $^{7}$Li signal intensity is reduced after the first cycle. We assign this observation to two main factors. First, $^{7}$Li NMR magnetization inside LFP is not visible in the spectra due to extreme line broadening caused by paramagnetic interactions. Second, once Li ions are incorporated into the SEI, the signal is lost because of the much longer relaxation times of $^{7}$Li in the solid state. The relaxation times used between scans in this setup are sufficient to polarize Li in LFP, the mobile electrolyte, and Li metal particles, but the times required to effectively recover magnetization of SEI components, such as Li in LiF, can be on the order of hundreds of seconds, which would be impractical in this experiment.

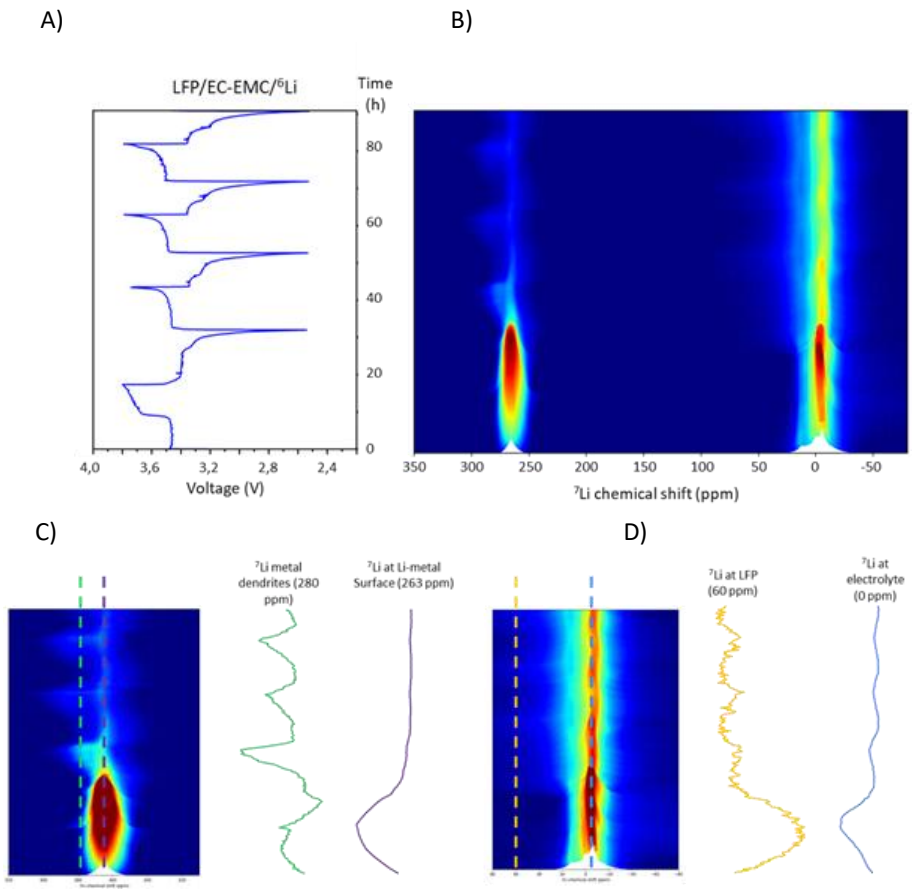




Funded by the European Union
OPINCHARGE

Figure 12. Operando $^{7}$Li NMR study of a cell comprising LFP and an isotopically labeled $^{6}$Li-metal counter electrode. $^{7}$Li NMR spectra were recorded during the electrochemical cycling shown in (A). Panels (C) and (D) display the intensity oscillations of signals assigned to Li metal and to the electrolyte/LFP, respectively.

## 1.1.3 Operando solid-state NMR studies on full cells

Within this project, operando solid-state NMR full-cell investigations were carried out. Figure 13 shows the corresponding experiments: (A) tracking the $^{7}$Li signal in a Si/Gr‖LFP full cell, and (B) monitoring the $^{13}$C NMR response of a $^{13}$C-labelled EC-based electrolyte in a Si/Gr‖LFP cell. In both cases, the results are consistent with the evolutions previously discussed for the half-cell configurations (Figures 5 and 9). As noted earlier, the $^{7}$Li spectra are dominated by the emergence of resonances between ~20 and 50 ppm, assigned to lithiation of the graphite component (Figure 13A). In the $^{13}$C experiment, the main observation is the clear initial decay of the solvent $^{13}$C signal, reflecting irreversible partial decomposition during the first charge associated with SEI formation (Figure 13B).

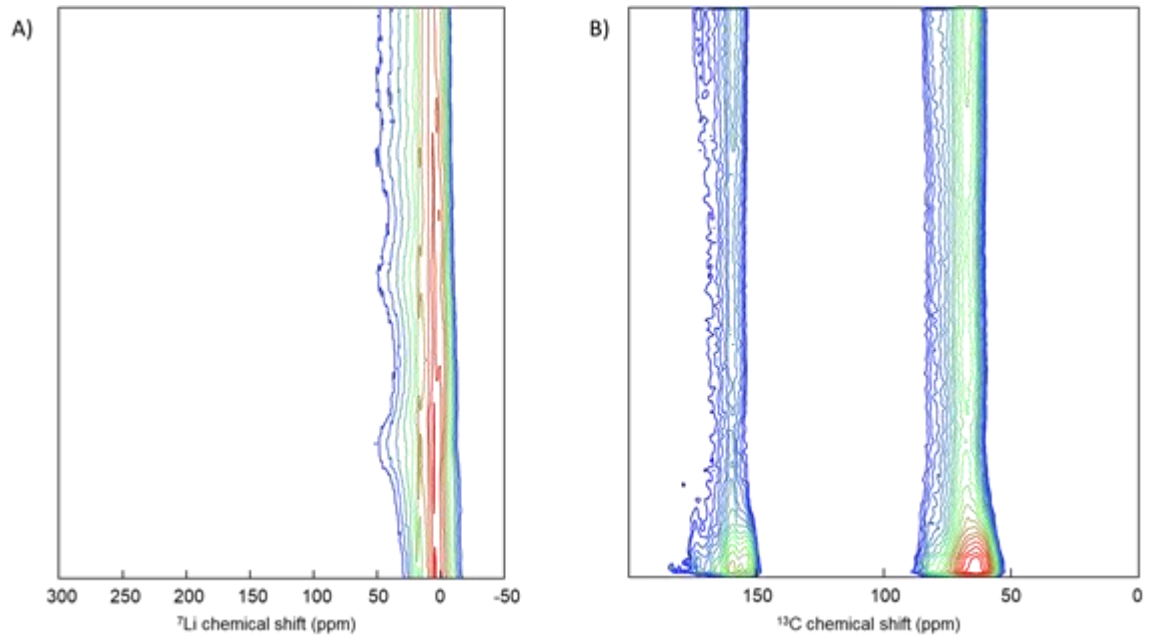


Figure 13. (A) Operando full-cell investigation of a Si/Gr electrode vs LFP using an FEC-based electrolyte. (B) Operando full-cell evolution of a $^{13}$C-labelled EC-based electrolyte in a cell composed of Si/Gr and LFP.

In future experiments within the OPINCHARGE project, *ex situ* characterization of the corresponding full cells will be performed, as it has proven valuable for identifying compounds formed at the interphases. SEI components are expected to be clearly resolved; however, determining CEI components remains challenging due to bulk magnetic susceptibility effects from the Fe-containing cathode material.


Funded by the European Union

## 1.1.4 Conclusions

1. Operando + ex situ ssNMR are complementary. Static operando ssNMR tracks processes in real time, while ex situ MAS provides spectral resolution for chemical assignments and SEI mapping. Together they deliver a structural–dynamic view that neither approach can provide alone.
2. SEI chemistry governs $Li^+$ transport. FEC-based electrolytes yield a more inorganic, LiF-rich SEI and higher effective interfacial exchange, whereas EC-rich SEI contains a larger organic fraction with broader but slower exchange—consistent with the distinct electrochemical responses.
3. EXSY/CP-EXSY resolve $Li^+$ exchange at the interface. Cross-peaks between SEI (~0 ppm) and lithiated silicon (~10 ppm) quantify interfacial exchange (e.g., τ_ex, k_ex), directly linking SEI composition to $Li^+$ transport and interfacial efficiency.
4. $^2H$ tracing reports SEI rigidity and heterogeneity. Operando $^2H$ signals decay early, indicating rapid formation of rigid organic SEI. Ex situ $^2H$ MAS separates at least three populations (rigid, semi-mobile, minor liquid-like), providing a direct handle on SEI mechanical/transport heterogeneity.
5. $^{13}C$ tracing identifies electrolyte-decomposition products. Beyond the EC solvent resonances (~65, ~155 ppm), additional intensity between ~10–50 ppm is consistent with ring-opened carbonate species (e.g., LEC/LEDC/LBDC), corroborated under MAS ex situ.
6. $^{6/7}Li$ tracing reveals heteroisotopic exchange and Li-metal morphology. Spontaneous metal|electrolyte isotope exchange is observed, and oscillations in the metal signal (~260–280 ppm) indicate increased accessible surface area (roughening, microstructures). The Li-metal NMR intensity reflects surface accessibility (skin depth), not bulk content.
7. Practical implication. Tuning SEI composition/architecture (e.g., LiF-rich outer layers with discontinuous organics) and controlling Li nucleation mitigate interfacial limitations. Isotopic-tracer ssNMR establishes actionable operando metrics (τ_ex, exchange amplitude, SEI rigidity) that connect SEI chemistry ↔ $Li^+$ transport ↔ electrochemical performance, guiding rational interface design.

## References:


[1] Grey, C. P.; Dupré, N. NMR Studies of Cathode Materials for Lithium-Ion Rechargeable Batteries. *Chem. Rev.* **2004**, *104* (10), 4493–4512.

[2] Pecher, O.; Carretero-González, J.; Griffith, K. J.; Grey, C. P. Materials' Methods: NMR in Battery Research. *Chem. Mater.* **2017**, *29* (1), 213–242.

[3] Bryce, D. L. NMR Crystallography: Structure and Properties of Materials from Solid-State Nuclear Magnetic Resonance Observables. *IUCrJ* **2017**, *4*, 350–359.

[4] Haworth, A. R.; et al. Solid-State NMR Studies of Coatings and Interfaces in Batteries. *Prog. Nucl. Magn. Reson. Spectrosc.* **2022**, *129–130*, 1–33.

[5] Ghorbanzade, P.; Pesce, A.; Gómez, K.; Accardo, G.; Devaraj, S.; López-Aranguren, P.; López del Amo, J. M. Impact of Thermal Treatment on the Li-Ion Transport, Interfacial Properties, and Composite Preparation of LLZO Garnets for Solid-State Electrolytes. *J. Mater. Chem. A* **2023**, *11*, 11675–11683.

[6] Ghorbanzade, P.; Pesce, A.; Armand, M.; Gómez, K.; Devaraj, S.; López-Aranguren, P.; López del Amo, J. M. Unveiling the Reactivity and the Li-Ion Exchange at the PEO–Li6PS5Cl Interphase: Insights from Solid-State NMR. *Small Structures* **2025**, e202400139.

[7] May, R. B.; et al. Rapid Interfacial Exchange of Li Ions Dictates High Coulombic Efficiency in Li Metal Anodes. *ACS Energy Lett.* **2021**, *6*, 1801–1808.

[8] Zhang, S. C.; et al. The Lasting Impact of Formation Cycling on the Li-Ion Diffusion between Li-Metal and SEI. *Sci. Adv.* **2024**, in press.

[9] Liu, M. D.; et al. Quantification of the Li-Ion Diffusion over an Interface by Exchange NMR. *Nat. Commun.* **2021**, *12*, 5882.

[10] Sanders, K. J.; et al. Quantitative Operando 7Li NMR Investigations of Silicon Anodes Reveal Intrinsic Nonequilibrium Behavior. *J. Am. Chem. Soc.* **2023**, *145*, 21505–21516.

[11] Šić, E.; et al. Towards Routine 7Li In Situ/Operando Solid-State NMR Studies of Commercial LIBs. *Appl. Magn. Reson.* **2024**, ahead of print.

[12] Grey, C. P.; Tarascon, J.-M. Sustainability and in Situ/Operando Characterization in Battery Research. *Nat. Mater.* **2017**, *16*, 45–56.

[13] Hope, M. A.; et al. Selective NMR Observation of the SEI–Metal Interface by DNP. *Nat. Commun.* **2020**, *11*, 2224.

[14] Gabrijelčič, M.; et al. Probing Sodium Structures and Dynamics in Hard Carbon Using 23Na Operando Solid-State NMR. *J. Mater. Chem. A* **2025**, *13*, 1042–1054.

[15] Liu, X.; et al. Solid-State NMR/MRI for Li/Na Batteries. *Adv. Mater.* **2021**, *33*, 2005878.

[16] Svirinovsky-Arbeli, A.; et al. Using NMR Spectroscopy to Link Structure to Function at the Solid Electrolyte Interphase. *Joule* **2024**, in press.

[17] Xu, C.; Lindgren, F.; Philippe, B.; Gorgoi, M.; Björefors, F.; Edström, K.; Gustafsson, T. Improved Performance of the Silicon Anode for Li-Ion Batteries: Understanding the Surface Modification Mechanism of Fluoroethylene Carbonate as an Effective Electrolyte Additive. *Chem. Mater.* **2015**, *27*, 2591–2599.

[18] Hsieh, Y.-C.; et al. Quantification of Dead Lithium via In Situ NMR Spectroscopy. *Joule* **2020**, *4*, 2338–2349.

[19] Ilott, A. J.; Chandrashekar, S.; Klöckner, A.; Chang, H. J.; Trease, N. M.; Jerschow, A.; Grey, C. P. Visualizing Skin Effects in Conductors with MRI: 7Li MRI Experiments and Calculations. *J. Magn. Reson.* **2014**, *245*, 143–149.

[20] Spiess, H. W. *Deuteron NMR—A New Tool for Studying Chain Mobility and Orientation in Polymers.* NMR—Basic Principles and Progress **1978**, 15, 55–214.

[21] Meier, B. H.; Ernst, R. R. Deuteron Spin–Lattice Relaxation in Molecular Crystals. *J. Chem. Phys.* **1979**, 71, 679–697.

[22] Michan, A. L.; Leskes, M.; Grey, C. P. Voltage Dependent Solid Electrolyte Interphase Formation in Silicon Electrodes: Monitoring the Formation of Organic Decomposition Products. *Chem. Mater.* **2016**, *28* (1), 385–398.

[23] Escher, I.; Freytag, A. I.; López del Amo, J. M.; Adelhelm, P. Solid-State NMR Study on the Structure and Dynamics of Graphite Electrodes in Sodium-Ion Batteries with Solvent Co-Intercalation. *Batteries & Supercaps* **2023**, *6* (2), e202200421.



Funded by the European Union

## 1.2 Development of an in-situ isotopic electrolyte exchange setup for operando neutron imaging and OEMS

Neutron imaging is a powerful tool to analyze the Li distribution in a lithium-based battery chemistry. However, in both in-plane and through-plane measurements, no distinction can be made between lithium contained within the active material (e.g. silicon) and the interphases formed at the active material-electrolyte interface.

Within OPINCHARGE, we address this challenge by developing a novel in-situ isotope exchange setup: after labelling interphases with a high-contrast isotope composition (e.g. $^{6}$Li) and removing all active lithium, we aim to replace the electrolyte with another isotopic (e.g. $^{7}$Li) composition of lower contrast for neutrons. This would allow to mainly observe the spatial distribution and/or average signal of the lithium contained within the initially formed, labelled interphases. Figure 2 shows the strategy to label the SEI of silicon electrodes.

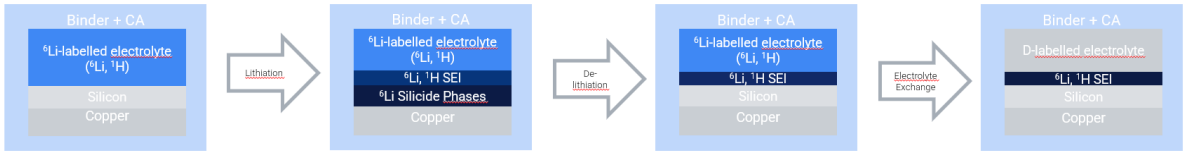


*Figure 2 Exemplary electrolyte exchange methodology for silicon. Attenuating phases are marked in blue, while phases invisible to neutron radiation are depicted in grey.*

In addition to the isotope exchange functionality, additional requirements such as compatibility with through-plane and in-plane neutron imaging as well as external compression had to be considered, requiring a step-wise development process. In the first phase, basic functionalities related to neutron imaging and applying currents under an external compression were tested. In phase two, pressure control of the cell is implemented, based on a syringe pump connected to a laptop with custom software allowing a constant pressure operation mode. Finally, the electrolyte exchange core feature is added to the final setup (Figure 3).

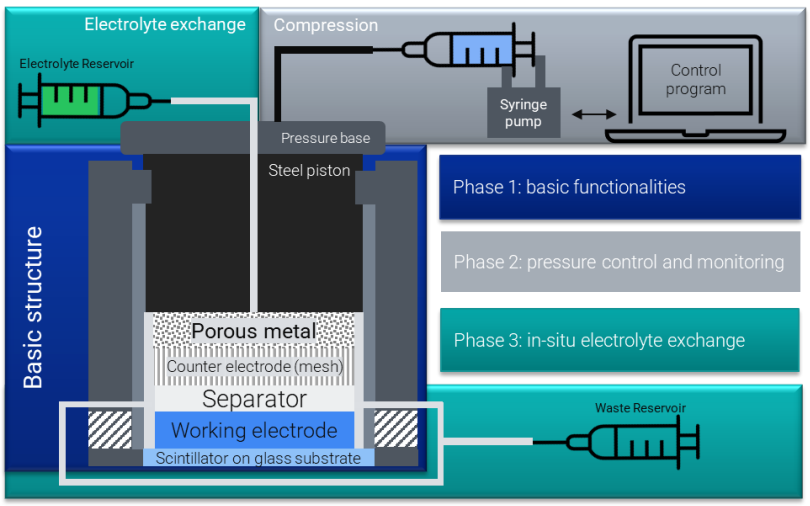


*Figure 3 Different components and related project phases of the electrolyte exchange setup.*



Funded by the European Union

In the following subsection, we present all goals that were initially defined for the setup.

## 1.2.1 Goals for OPINCHARGE electrolyte exchange setup

These are requirements specific to the electrolyte exchange system, which operates in conjunction with the battery cell:

1. System Design
    - The system must facilitate the controlled exchange of electrolyte for the cell.
    - Reservoirs: Two separate electrolyte reservoirs must be connected to a peristaltic pump via valves, enabling precise flow control into the cell.
    - Waste Management: Two waste reservoirs must collect the electrolytes separately.
2. Volume and Speed Requirements (System-Specific)
    - The system must handle electrolyte volumes between 50-200 µL, ensuring complete exchange within 60 seconds or faster.
3. Electrolyte Properties (System-Specific)
    - The system must account for electrolyte viscosities ranging from 0.7 to 1.5 cP at room temperature when designing tubing and pump flow rates.
4. Maintenance and Cleaning
    - The system must allow easy disassembly and cleaning, ensuring no contamination between experiments.

**Battery Cell Requirements**

These are the requirements specific to the battery cell itself:

1. Electrolyte Exchange Mechanism
    - The volume of the chamber containing the cell stack should be designed to limit the total electrolyte volume within this region to a maximum of 200 µL, minimizing the electrolyte volume that needs to be exchanged.
    - Electrolyte Properties: The cell must accommodate carbonates and ether-based electrolytes containing typical concentrations of 1M $LiPF_6$ and other lithium salts.
    - The cell must allow for complete electrolyte removal without simultaneous addition, to enable specific experimental requirements.
2. External Pressure Application
    - The cell must support mechanisms to allow defined external pressure application up to 10 bar.
    - The compression should ideally be monitored throughout cycling via a force sensor (e.g. load cell).
    - Special care must be given to the homogeneity of the compression, to avoid inconsistencies during experiments.
    - To be considered: For neutron capture imaging, the pressure can only be applied from one side since the working electrode contacts a scintillator fixed to a metal plate.
3. Material Specifications
    - The materials used for the sides of the cell stack (perpendicular to the working electrode) must have low neutron absorption to support neutron-based experiments.
    - The electrical connections for applying a current must be designed in a way that is compatible with working electrode (e.g., copper foil) being in contact with an electrically insulating glass substrate on the side facing the outside of the cell stack.
4. Optical Specifications


Funded by the European Union

- The housing of the cell on the working electrode side should be designed in a way that permits neutrons to enter from a low angle (< 30°)

5. Environmental Requirements
   - The cell must operate under inert conditions with <0.1 ppm $H_2O$ and <0.1 ppm $O_2$, or in a vacuum of $10^{-3}$ bar.
   - Sealing Mechanisms: Appropriate sealing must ensure inert or vacuum conditions are maintained, with HPLC fittings strongly favored.
6. Size and Portability
   - The cell must be portable, i.e. transportable by hand.
7. Compatibility with OEMS
   - The cell should ideally be compatible with Online Electrochemical Mass Spectrometry (OEMS), meaning that the connectivity with the OEMS system (inlet and outlet) should align with the OEMS Cell currently used at PSI. If this cannot be combined with the previous requirements, a second cell needs to be developed, with all requirements except for those particularly related to neutron absorption.

**Shared Requirements (Cell and System)**

These requirements are applicable to both the cell and the system, as they depend on the integration and overall design:

1. Material Specifications
   - The materials used must be chemically inert to the electrolytes and resilient to applied pressures, fluid dynamics, and inert or vacuum conditions
2. Safety
   - Both components must comply with laboratory safety standards.

## 1.2.2 CADs and pictures of setup

### 1.2.2.1 Cell structure

In Figure 4a-b, schematic depictions of two novel cells are shown – one basic variant allowing to perform neutron experiments under controlled compression, and one variant that additionally incorporates an electrolyte exchange functionality. In both, the cell can equip a glass chip with a scintillator coating on one side, which is needed for neutron capture imaging experiments (see next task). For tests without electrolyte exchange, a steel piston is pushed at the electrode stack (e.g. Cu current collector, separator and counter electrode) using a simple, 3D-printed part holding a screw (Figure 4c) during cell assembly. For electrolyte exchange tests, the steel piston is fitted with a channel for a tube, which is used to deliver the electrolyte to the cell stack. To achieve a homogeneous spreading across the surface, a porous metal disk is added, and a mesh counter electrode is used with the intention to allow a quicker diffusion to the (porous) separator and working electrode.


Funded by the European Union

a) b)

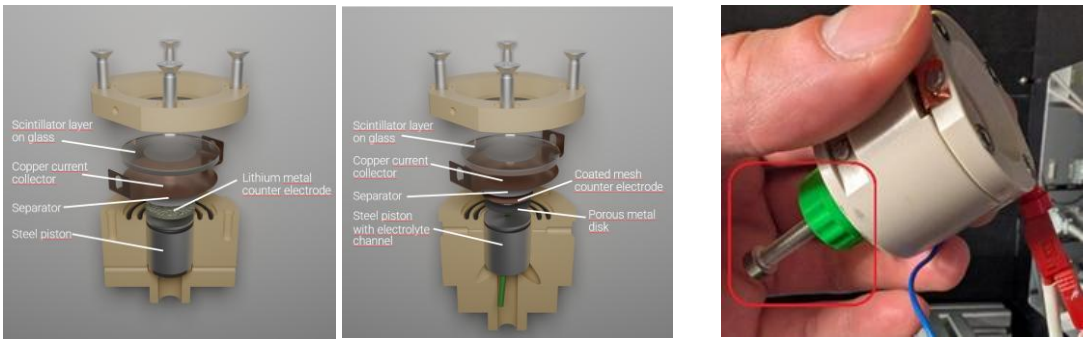


*Figure 4 a) Cross-sections of the OPINCHARGE cell without (left) and with (right) electrolyte exchange feature; (b) shows a photo of the basic cell and the screw used for precompression.*

#### 1.2.2.2 Compression via syringe pump

For controlled compression on the electrode stack, a setup consisting of a pressure base (see Figure 5) connected to a syringe via tubing is used. This syringe is fixed in a syringe pump system, which can be controlled by a custom program, currently still under development.

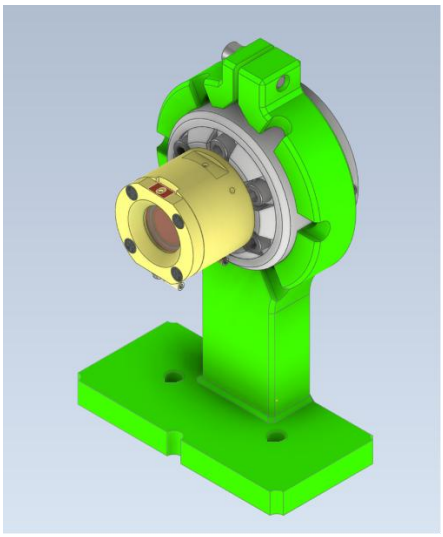

*Figure 5 OPINCHARGE cell with compression base and 3D-printed holder for neutron imaging. The compression base is connected to a syringe pump.*

## 1.2.3 Example of experimental procedure

In preparation for the first tests with the electrolyte exchange cell, a procedure has been drafted.

1. The cell is assembled in the glovebox. To ensure that all electrodes are well aligned and do not move during the transport, the cell is precompressed using an auxiliary system consisting of a screw and a 3D printed part (Figure 4c).
2. The electrolyte reservoir syringe is filled with electrolyte, attached to the cell upside down to avoid electrolyte contacting the counter electrode prematurely and fixed in a 3D printed holder, which also holds the cell, as shown in Figure 6.



Funded by the European Union

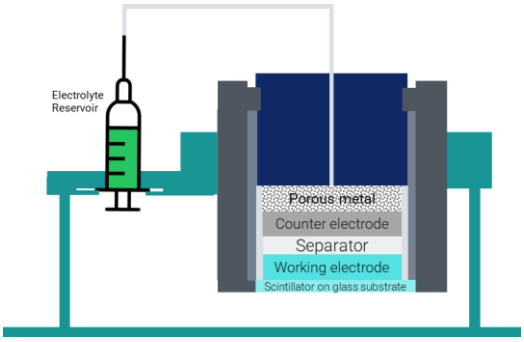


*Figure 6 3D-printed holder preventing the cell components from moving during removal of auxiliary compression system as well as the premature injection of electrolyte into the cell.*

3. The waste reservoir syringe is attached to the cell.
4. The cell in its holder is removed from the glovebox and transferred to the experimental setup.
5. The auxiliary system is carefully removed and replaced by the syringe pump-controlled compression system.
6. Using the custom software developed for the cell, the syringe pump is operated and used to apply a constant force on the piston, which transmits it further to the working electrode. The force is monitored by a load cell located outside of the cell.
7. The cell is connected to a potentiostat, the electrochemical experiment starts and the output of the load cell is registered and automatically converted to pressure. The syringe pump is controlled by a laptop with custom software, and automatically keeps the compression constant
8. After the first charge and discharge cycle, the waste reservoir syringe is pulled to create a mild vacuum and remove the electrolyte from the cell. At the same time (or subsequently), the reservoir syringe is being pressed to introduce an additional (relatively neutron-invisible) electrolyte into the cell.

### 1.2.3 Conclusions

To summarize, this section describes:

- Development of a novel setup allowing to apply a defined external pressure, perform neutron imaging in-plane and through-plane as well as exchange the electrolyte in-situ
- Requirements, CADs, and photos of setup components
- Exemplary procedure for applying and sustaining a defined compression and exchanging the electrolyte

## 1.3 Operando neutron imaging in combination with isotope labelling

Neutron imaging provides a powerful tool to study lithium-ion batteries[1–3]. Unlike X-rays which interact primarily with heavy elements, neutrons are sensitive to certain light elements such as H and Li. In particular, $^{6}$Li has a large neutron cross section of 861 barns thanks to the nuclear reaction $n + {}^{6}Li \rightarrow \alpha + {}^{3}H$ [4]. With $^{6}$Li isotope enrichment, neutron radiography (NR) can detect lithium



Funded by the European Union

distribution with a thickness precision down to 1 µm and a spatial resolution in the 10 µm order of magnitude.

However, even when employing 6Li, NR meets a limitation when resolving very small quantities: For a 100 nm 6Li layer, only 0.07% of incident neutrons are absorbed, which generally results in too low contrast to be detected against the intrinsic Poisson noise in the background[5]. Another restraint comes regarding imaging lithium plating and stripping in lithium metal batteries with through-plane transmission. If one attempts to obtain a 2D map of plated lithium on the current collector, the lithium metal electrode on the opposite end would also contribute to the signal. To avoid collimation of the lithium electrode and plated lithium, Eric et al. designed an annular electrode cell for operando NR measurements[6]. A major drawback, however, is the necessity to use an annular 6Li counter electrode to allow for neutrons to pass through. Consequently, most of the plated lithium is observed at the electrode edges, and the impact of pressure is neglected, which has been shown to play a crucial role in the efficiency of lithium plating and stripping.

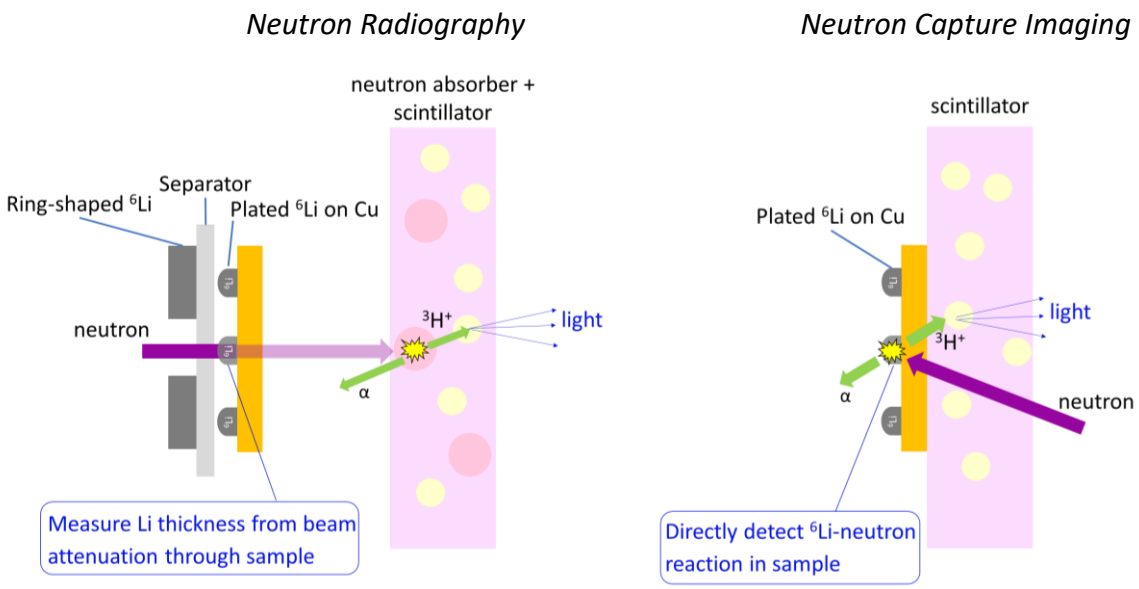


*Figure 7 Schematic of the principles of neutron radiography (left) and neutron capture imaging (right). In NR, the thickness of $^{6}$Li as the major attenuating species in the sample is obtained by measuring the intensity of the attenuated beam. In NCI, the thickness of 6Li in the sample is obtained by measuring detecting the charged secondary particles produced by neutron capture reactions inside the sample.*

Supported by the OPINCHARGE project, we developed a novel neutron imaging approach based on directly detecting the neutron capture by $^{6}$Li in the cell instead of measuring the attenuation. The new method is named neutron capture imaging (NCI). A comparison between the principles of NR and NCI is shown in Figure 7. In NR, the transmitted, the scintillator (doped by neutron absorbers such as $^{6}$Li and Gd) receives the transmitted, attenuated neutron beam and produces light output. In NCI, the scintillator does not react with the neutron beam, but only with the $^{3}H^{+}$ secondary particles produced at the plated lithium on the Cu current collector.

While the contrast in absolute terms is the same as for radiography, the neutrons which are not captured by $^{6}$Li in the sample are not detected, resulting in a near-zero background. This allows for higher signal-to-noise ratios (SNRs) and unprecedented $^{6}$Li sensitivity. Since the transmitted neutrons are no longer measured, the neutron beam can be incident from any angle, offering flexibility for the cell design (e.g. circular $^{6}$Li metal electrodes). Moreover, there is no need for a collimated neutron beam, meaning that the intensity of the beam could be increased significantly by using measurement


Funded by the European Union
OPINCHARGE

positions near the neutron sources and/or by using focusing guides. Images will not be affected by background scattering neutrons either.

## 1.3.1 NCI setup development

A number of NCI setup configurations were proposed and tested, and the specifications are shown in Table 1. Setup A is the conventional NR configuration. Setup B is the first NCI test with the same optical configuration and CCD camera as setup A, which offers a direct comparison. Setup C utilizes the special TimePix 3 Camera which records individual photon arrivals with nanosecond time resolution[7]. The photon statistics are processed to neutron events with a centroiding algorithm to obtain improved spatial resolution and further suppressed background noise. To have the neutron beam reach the plated lithium before the lithium metal anode, the MIDI camera box has to be oriented in the way that the neutron beam hits the box and mirror first, which attenuates the neutron beam. To maintain high neutron flux, we proposed setup D with a customized optical setup which places the cell directly in front of a relay lens systema and the TimePix 3 Camera. The ZnS:Cu scintillator was also replaced by ZnS:Ag whose light output, despite being lower in general, has wavelengths which match better with the optimal performance wavelength of the TimePix 3 Camera's intensifier (Photonis Cricket).

*Table 1 Specifications for four setups tested. The NR setup is also included to offer a cross-validation*

| | Method | Optical | Scintillator | Camera |
|---|---|---|---|---|
| A | NR | MIDI box | $Gd_2OS_2$:Tb 30µm | Andor Ikon-L CCD |
| B | NCI | MIDI box | ZnS:Cu 50µm | Andor Ikon-L CCD |
| C | NCI | MIDI box | ZnS:Cu 50µm | ASI TimePix 3 |
| D | NCI | Customized | ZnS:Ag 50µm | ASI TimePix 3 |

It was found that the best sensitivity is offered by setup D: NCI with customized optical setup, ZnS:Ag scintillator, and TimePix 3 Camera. Figure 8 shows a picture of the up-to-date setup D for NCI. The camera, connected to the intensifier and relay lenses, is mounted onto a linear stage for focusing. The cell holder is placed in front of the relay lenses, and the scintillator is incorporated into the cell. All components are stored in a semi-lighttight anodized aluminum box (which is still to be upgraded).


Funded by the European Union

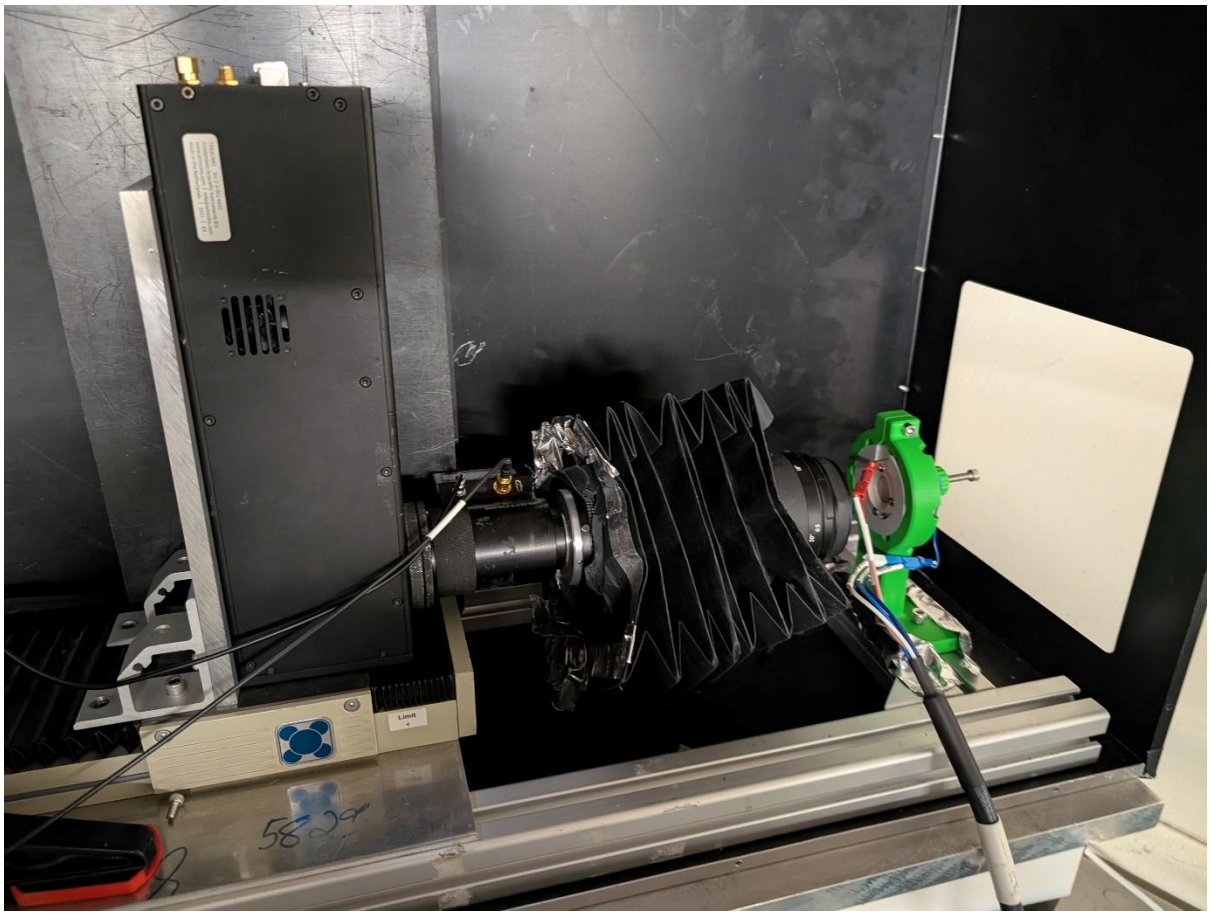

*Figure 8 Setup D: NCI configuration with TimePix 3 Camera, linear stage, a relay lens system and the cell holder, all in a semi-lighttight anodized aluminum box.*

## 1.3.2 Validity tests on ex-situ electrochemically plated $^{6}$Li samples

To prove the validity of the NCI approach and find the best setup configuration, test measurements were conducted on ex-situ electrochemically plated $^{6}$Li samples of average thicknesses ranging from 10μm to 10nm and a diameter of 12mm. The results are shown in Figure 9. With similar neutron flux exposures, both NR and NCI offered sufficient sensitivity for the 10μm and 1μm samples. However. setup D saw a saturation in the image due to both the $^{6}$Li layer is too thick at some positions (greater than 40μm) and high light output exceeding the maximum photon hit rate of the TimePix 3 Camera (80 Mhits/s). For the 100nm and 10nm samples, NR was not able to provide any sensible contrast as the $^{6}$Li signal is largely overridden by background noise. NCI with CCD camera (setup B) was able to resolve the hundred-nanometer-thick $^{6}$Li deposits in the 100nm sample, but the noise was still too high for the 10nm sample. With additional noise suppression offered by TimePix 3 Camera and the centroiding algorithm, NCI was able to resolve features in the 100nm and 10nm samples nicely, improving the $^{6}$Li sensitivity by at least tenfold.



Funded by the European Union

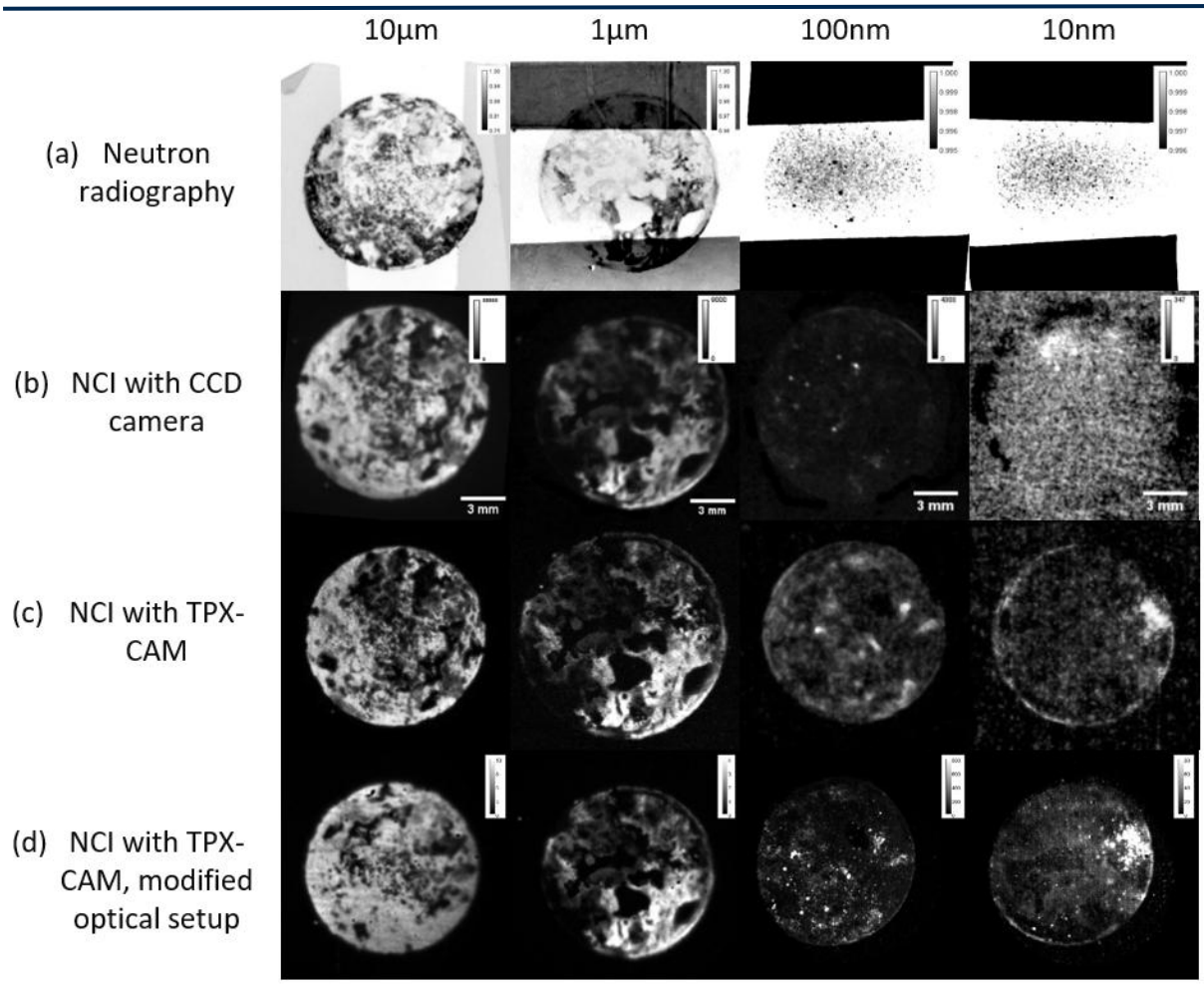


*Figure 9 NR and NCI measurement results of four ex-situ electrochemically plated $^{6}$Li samples. $^{6}$Li of average thicknesses of approximately 10µm, 1µm, 100nm, and 10nm was plated on Cu substrate, then sealed in 10µm-thick Cu foil bags to prevent contamination by air. For each sample, measurements were conducted at the same beamline (ICON or BOA at SINQ, PSI). Measurement times were either kept constant or adjusted according to the flux difference at different sample positions to obtain the same exposure for fair comparison.*

## 1.3.3 Operando measurements

Operando tests were then conducted on an electrochemical cell adapted from X-ray diffraction purposes, before the new pressure-controlled, electrolyte exchange cell was commissioned. $^{6}$Li-labelled carbonate electrolyte was prepared by dissolving $^{6}LiPF_6$ (Sigma-Aldrich, 99,99%, battery grade) in 1:1 EC (ELyte)/DMC (E-Lyte). Plating and stripping was performed using a Biologic SP 150 potentiostat by applying a current density of 0.5 mA/cm$^2$ for 1.58 h, and -0.5 mA/cm$^2$ until a cutoff voltage of 0.5 V vs $Li^+$/Li was reached. The imaging results and the electrochemical data recorded by the potentiostat are shown in Figure 10.

Generally, it could be observed that the average intensity of images evolved in a pattern that aligned well with the electrochemical protocol: while no lithium was detected in the initial Open Circuit Voltage phase (Figure 10 c), the intensity in some areas increased during the first plating process (Figure 10 d) and was maximal at the end of plating (Figure 10 e). Then, the removal of lithium was reflected by a decrease in signal (Figure 10 f) until the stripping step was finished (Figure 10 g). At this stage, it was observed that around 68% of the lithium had been removed. These are thought to consist of electrochemically passive “dead” lithium and lithium in the Solid Electrolyte Interphase (SEI). Finally, another plating step resulted in the additional electrochemical deposition of lithium ( h), this time not reaching the same signal intensity due to the shorter plating time. We note that the cell used for the


Funded by the European Union
OPINCHARGE

experiment is not ideal as the mechanism of applying (under-)pressure on the layers may result in damage (e.g. wrinkles) of the thin Cu foil, which might result in an inhomogeneous contact inside of the cell and locally increase electrical resistance. To eliminate this as a reason for inhomogeneous plating, as seen in the operando images, future operando tests should be conducted using a cell that can be homogeneously compressed by an external force rather than underpressure applied by a syringe.

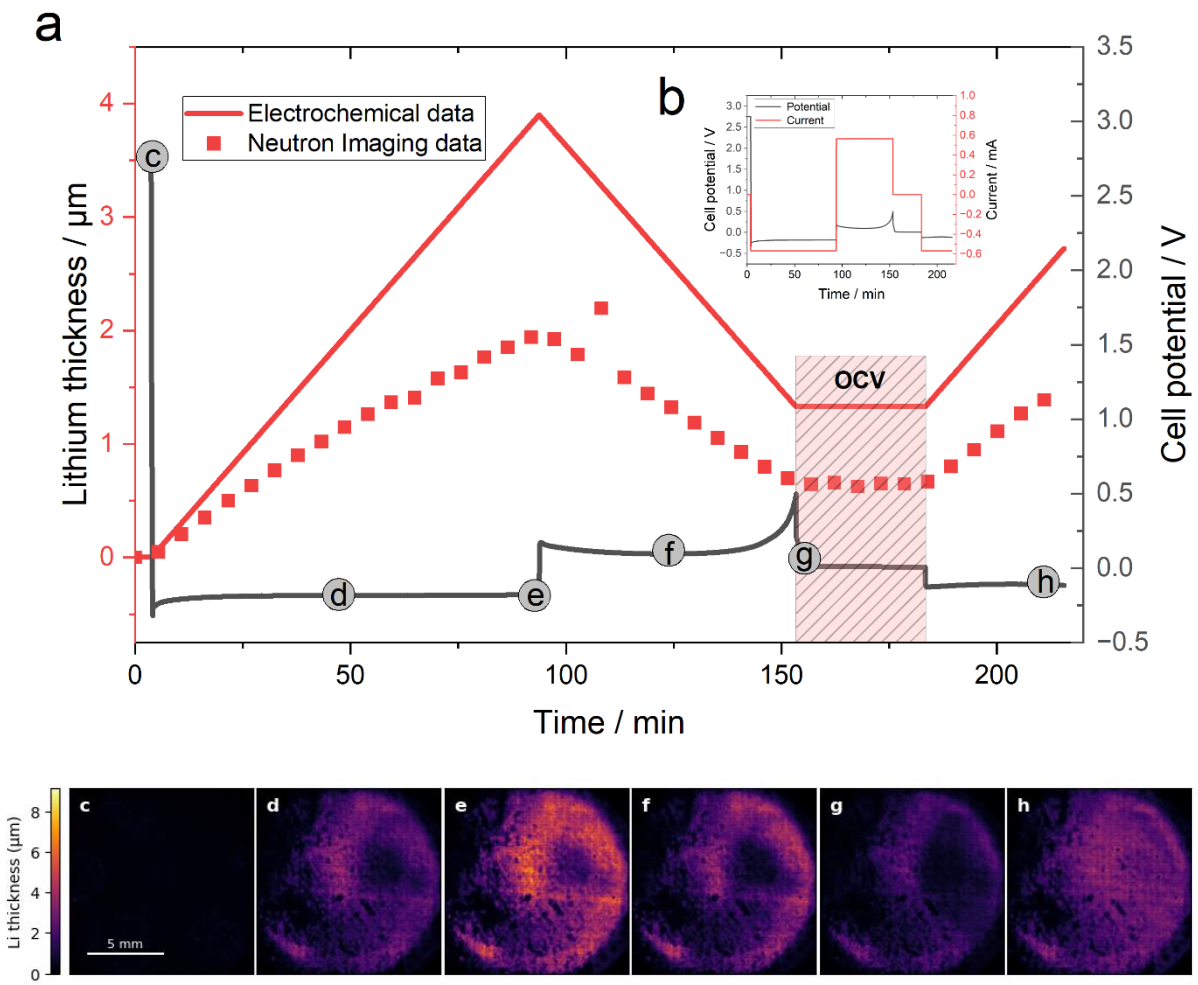


*Figure 10 Results of operando NCI measurements of the electrochemical cell. Data were processed with 5-minute acquisition windows. (a) Average $^{6}$Li thicknesses calculated from NCI data, calibrated by the NCI measurement of a 1µm thermally evaporated uniform $^{6}$Li layer, and from the electrochemical data. (b) Raw electrochemical data recorded by the potentiostat program. (c-h) NCI images at selected phases as marked on (a).*

As the thickness calculated from the capacity can only be seen as an upper theoretical limit, it is not surprising that the thickness calculated from neutron imaging is lower, as it also takes side reactions such as electrochemical deposition of the electrolyte into account. Decomposition products of such reactions also contain lithium but are likely to exhibit a considerably lower lithium density than metallic lithium. It could also be due to calibration errors, as the reference measurement of the 1µm thermally evaporated layer was not fixed at the exact same position, leading to potentially different neutron fluxes.

## 1.3.4 Resolution measurement and SRIM simulations

While the $^{6}$Li thickness sensitivity of NCI was demonstrated with the eletrochemically plated samples, spatial resolution is estimated from the 1µm thermally evaporated sample which provide a sharper


Funded by the European Union
OPINCHARGE

edge. The line spread function at the egde was computed with a Voigt fit, from which the spatial resolution was estimated to be 103μm, close to the raw pixel size of 109μm thanks to the centroiding algorithm. An important limitation of the NCI method is the resolution limit caused by the isotropic travelling of $^{3}H$ particles once they are produced in the $^{6}Li$-neutron capture reactions.

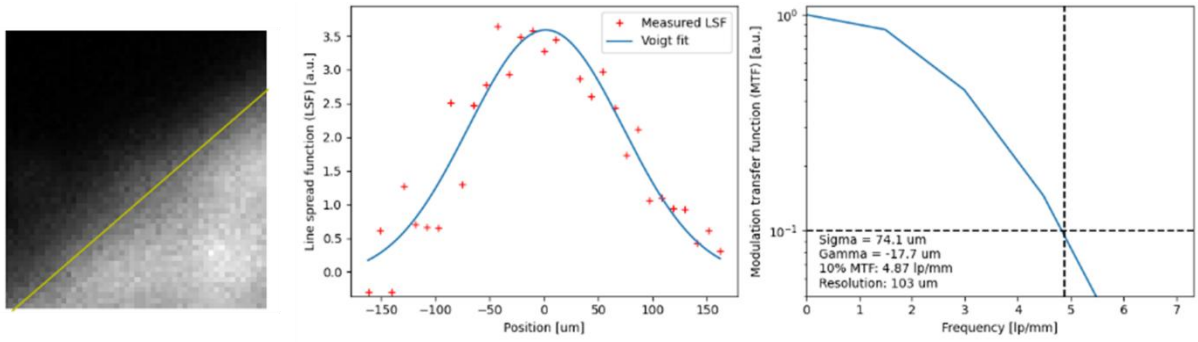


*Figure 11 Spatial resolution estimation of the current NCI setup from the 1μm thermally evaporated sample. The resolution is estimated to be around 103μm, which is close to the raw pixel size of 109μm due to the centroiding data treatment.*

To verify the resolution limit of our system, Monte-Carlo simulations of the $^{3}H$ particles were performed with the SRIM software[8]. The results are shown in Figure 12. In each simulation, $10^{5}$ $^{3}H$ particles were released isotropically, and those which travel through the $^{6}Li$ and Cu layers were recorded. The point spread function of the $^{3}H$ arrivals was then estimated, and the corresponding resolution limit was computed as the 10% MTF (modulation transfer function) cutoff. For our current operando setup of 10μm Cu foil and $^{6}Li$ under 5μm, it was shown that the resolution limit is around 18μm to 30μm. It is clear that our NCI system is now optically limited (by the camera pixel number and size), rather than intrinsically limited by the NCI physical processes.

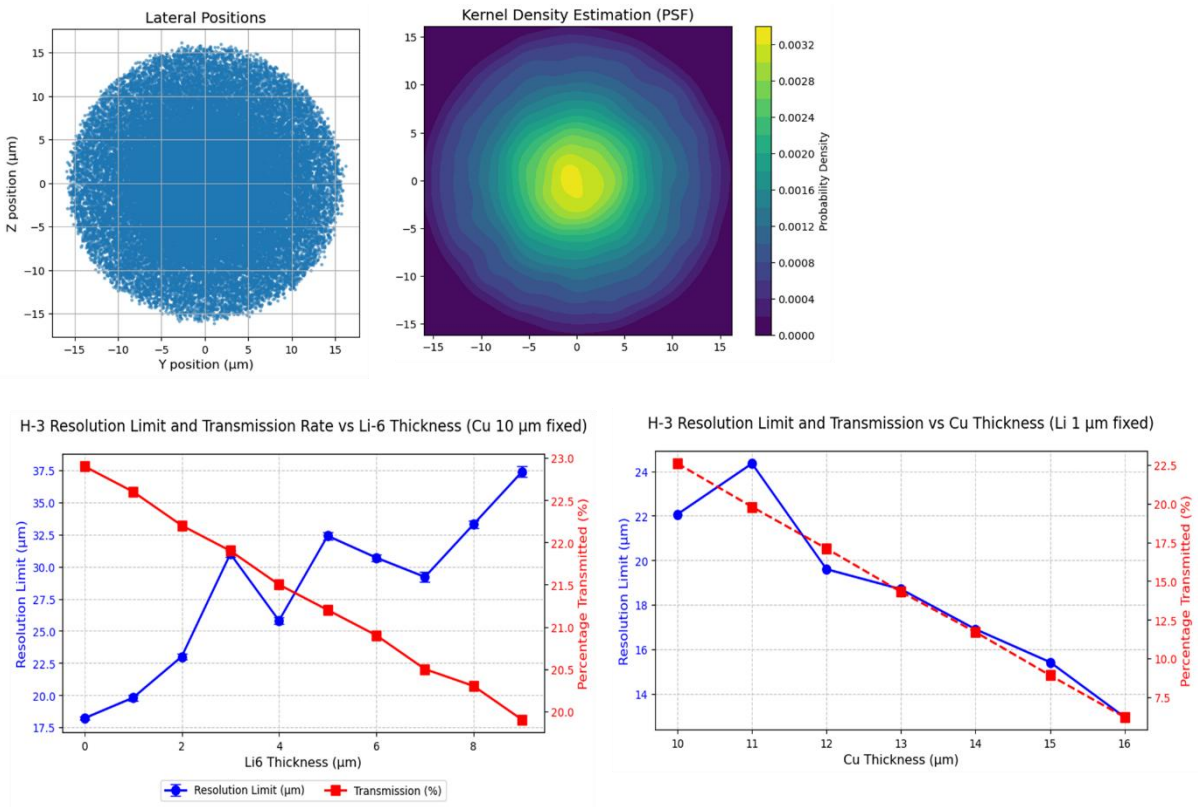


*Figure 12 SRIM Monte-Carlo simulation of the spread of secondary $^{3}H$ particles reaching the scintillator. In each simulation $10^{5}$ ions travelled isotropically in all direction, and the ones which transmit through the $^{6}Li$ and Cu layers were recorded. The thicknesses of the $^{6}Li$ and Cu layers were varied and changes in the resolution limit and transmission rate are demonstrated.*



Funded by the European Union

# 1.4 Development of an in-situ isotopic electrolyte exchange setup for operando neutron imaging and OEMS

## 1.4.1 Electrolyte Labelling strategy

The envisioned use of OEMS to elucidate SEI and CEI formation of high-energy density electrodes is paired with a strategy to increase the selectivity of the technique towards selected electrolyte components. $^{13}$C-labelled carbonate solvents and additives should clarify questions regarding the deconvolution and origin of gases such as $C_2H_4$, CO and $CO_2$. Preceding the use of isotope-labelled compounds are studies in which cells are built with electrolytes composed of single solvents, facilitating an initial assignment of gases to electrolyte components (Figure 13, Phase 1). Subsequently, employing LP30-based electrolytes composed of one $^{13}$C labelled component should contribute to the better understanding of CO and $C_2H_4$ evolution in realistic electrolyte compositions (Figure 13, Phase 2). Finally, the gas evolution of additives will be selectively studied by following the $^{12}$C gas signals evolving from the non-labelled additive compounds in presence of the $^{13}$C-labelled main solvents EC and DMC (Figure 13, Phase 3).

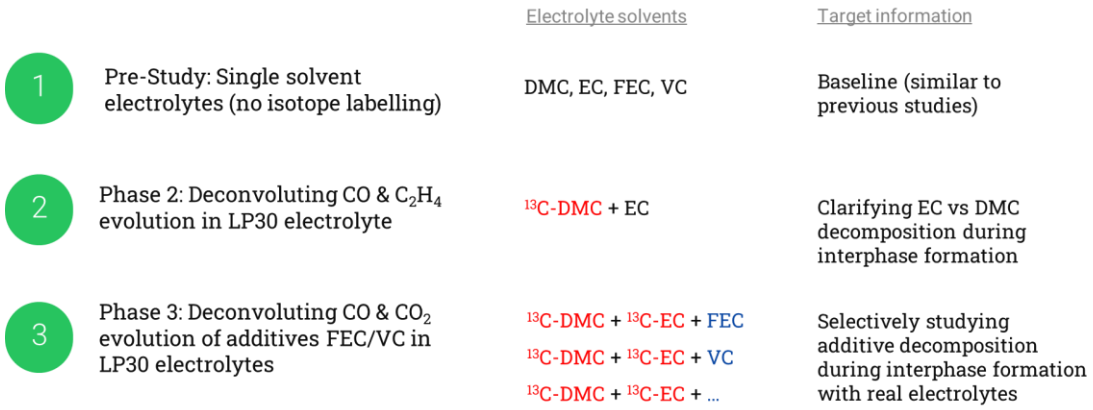


*Figure 13 Overview of OEMS experiments involving isotope-labelled compounds. Labelled electrolyte components are marked in red, and a summary of the target information is given on the right.*

## 1.4.2 LMFP Gassing studies

In a system with the standard lithium-ion battery electrolyte LP30, the gassing behavior of LMFP was studied, using the non-gassing electrode material LFP as a counter electrode, which was previously delithiated electrochemically to 75 % by controlling capacity to achieve a stable potential vs the working electrode. The LMFP working electrodes were obtained by blade-coating on an Aluminum mesh.

It was observed that the LMFP is not exhibiting any gas evolution within the operational voltage window of 2.4 V – 4.4 V (Figure 14a). Only when increasing the potential to 4.6 V vs $Li^+$/Li or higher, $CO_2$ is formed, as a result of electrolyte decomposition (Figure 14b).


Funded by the European Union
OPINCHARGE

a.)

b.)

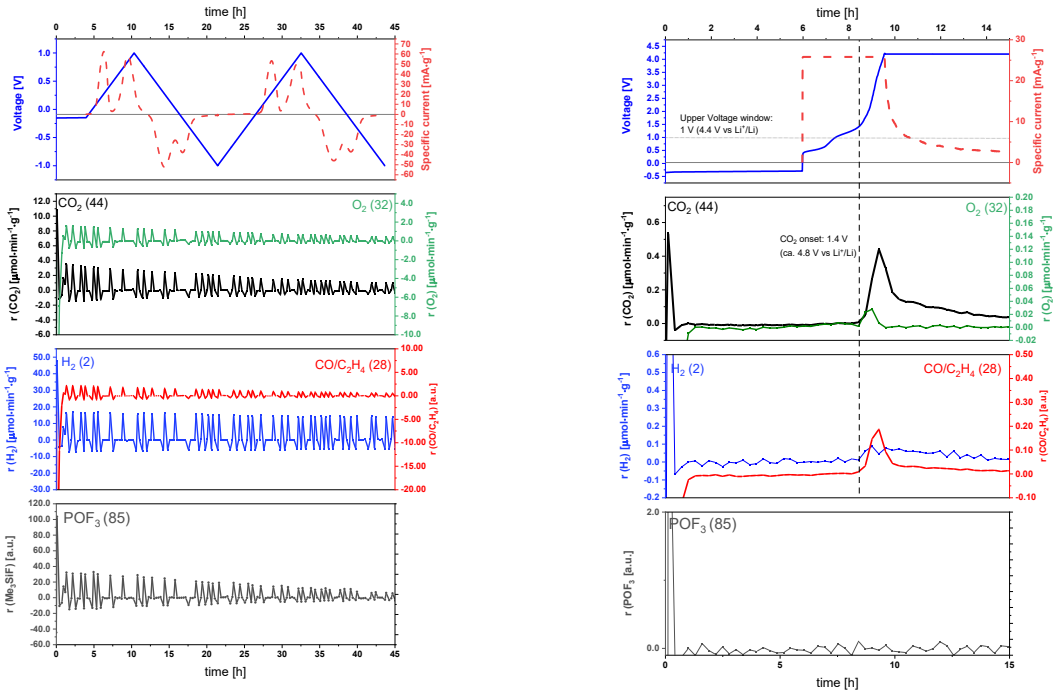


*Figure 14: OEMS tests of LMFP in full cell configuration, with LP30 as electrolyte; a) CV between 4.4 V and 2.4 V vs $Li^+$/Li, 50 mV/s. The test was carried out with three cells; b) Overcharging experiment, with C/3 constant current step charging to 4.6 V vs $Li^+$/Li and subsequent voltage hold. The experiment was carried out with three cells.*

Therefore, isotope labelling is not necessary to track the gas evolution of additive decomposition during interphase formation. Instead, the strategy described in 0 is considered more informative in the context of Silicon electrodes (next section).

# 1.4.3 Silicon Gassing studies

## 1.4.3.1 Cycling tests

Long-term cycling tests of silicon half-cells, comparing a variety of electrolytes (Figure 15a) and two binders (Figure 15b) were carried out to identify trends of cycling stability related to additive addition and binder selection, as a higher cycling stability can related to a more stable SEI.

FEC effectively improves the capacity retention with increasing concentration up to fully substituting EC; an opposite trend is visible when transitioning to VC, which can even result in lower capacities than the reference LP30 electrolyte, if the ratio of VC to the active material exceeds a certain value.

With another set of cells, the impact of the binder on the cycling stability was investigated. With the chosen electrode properties and experimental conditions, a PAA binder seems to clearly outperform a NaCMC binder at the same weight percentage. This may be linked to SEI formation, as attempted in a preliminary set of OEMS experiments (next section).



Funded by the European Union

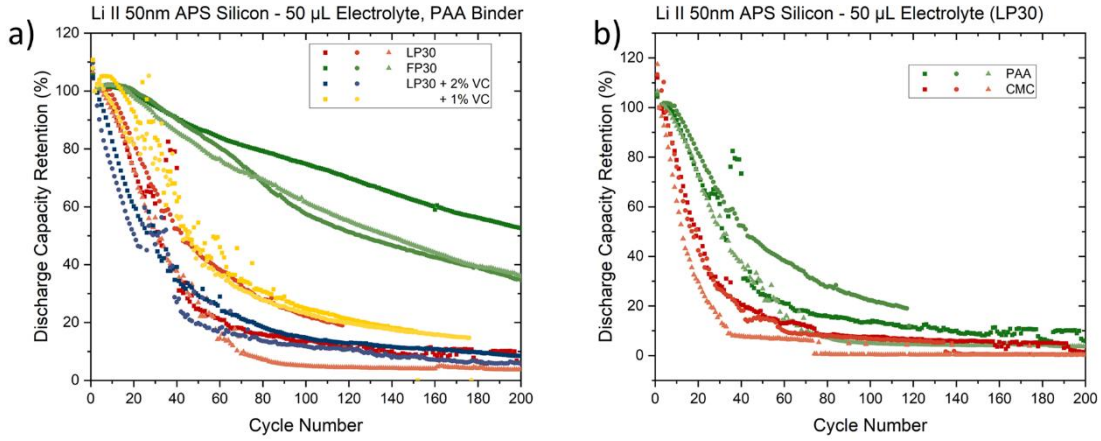


*Figure 15: Cycling data of silicon cells paired with different a.) electrolytes and b.) binders. FP30 is an analogue to LP30 with EC being fully substituted by FEC. All cells were cycled under C/10 charge and discharge rate, with an initial cycle under C/20 for the purpose of SEI formation.*

### 1.4.3.2 Preliminary OEMS tests

In preliminary OEMS studies with electrodes manufactured using a previously established bar coating process, the goal was to identify the impact of the choice of counter electrode and the binder on the gas evolution.

Moving from a half cell to a full cell (Figure 16 a and b) using a partially delithiated, non-gassing LFP counter electrode mainly impacts the hydrogen evolution, as would be expected from the high chemical reactivity of metallic lithium towards $H_2$ sources such as residual water. This chemical reactivity may also explain why most of the hydrogen evolution is observed at higher potentials between 1.66 V and 0.34 V vs $Li^+/Li$, while in the full cell, most of the hydrogen is evolved at a potential as low as 0.17 V vs $Li^+/Li$, overlapping with the potentials at which $C_2H_4$ and possibly CO is evolved, which are typically associated with the decomposition of EC as part of the SEI formation process.[9]

As for the impact of the binder (Figure 16 c and d), the onset potentials are similar for $C_2H_4$, CO and $CO_2$ while they differ considerably for $H_2$. The $H_2$ evolution starting at 1.68 V vs $Li^+/Li$, which is clearly observed for the electrodes with the PAA, binder may be associated with the higher proton concentration introduced by the binders during electrode preparation, as reported by previous studies.[10]

For more quantitative studies of the gasses evolved, a novel electrode manufacturing process (see next section) was developed to obtain a more homogeneous loading for each electrode. Once the trends identified in the preliminary studies are confirmed with these electrodes, the labelling strategy elaborated before will be introduced to bring further clarity on the origin of the gasses and improve our understanding of the SEI formation process, the impact of the counter electrode and of the binder.


Funded by the European Union
OPINCHARGE

a) Counter electrode study

Lithium Metal

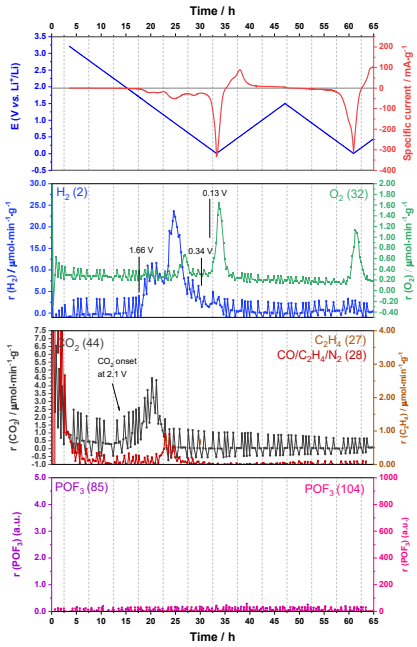


LFP

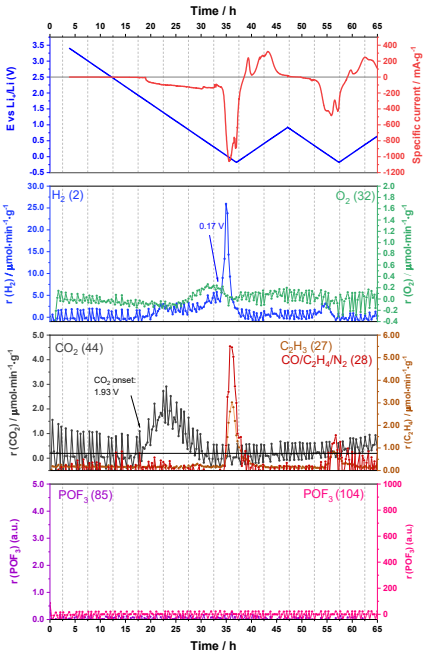


b) Binder study

NaCMC

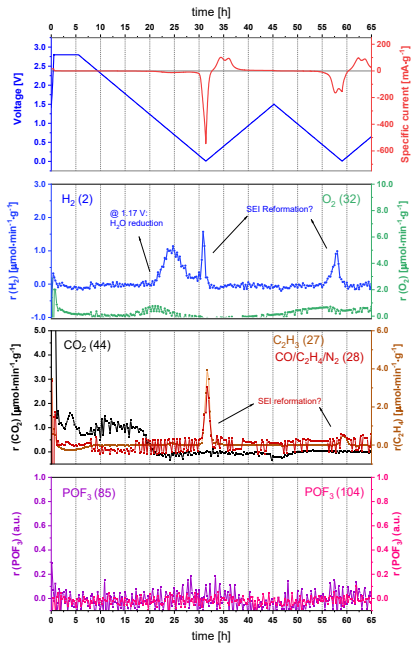


PAA

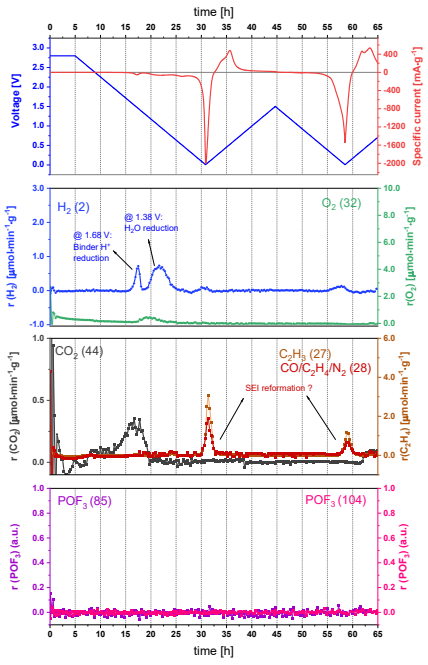


*Figure 16: Preliminary OEMS data of silicon electrodes; a) Comparison of half-cells and full-cells (using partially delithiated LFP as counter electrode). The $O_2$ signal in the half-cell indicates residual oxygen not sufficiently removed during the equilibration phase; untight cells may be explain the unstable signals of most gasses; b) A binder study comparing the impact of NaCMC and PAA, at the same weight percentage. The $CO_2$ signal has not been calibrated correctly and onset potentials could therefore not be identified clearly.*



Funded by the European Union

### 1.4.3.3 New electrode manufacturing route

Previously, Si electrodes were produced by applying a highly viscous slurry to Cu mesh (3CU6-031FSRx12', Dexmet, USA) and then manually bar coating it (Figure 17 a). This approach has the drawback that the loadings usually turn out to be highly inhomogeneous across the mesh surface, and that the results highly depend on the person doing the coatings, as it is hardly possible to accurately control the pressure applied to the mesh and the speed of coating. Furthermore, the loadings obtained have a rather large error due to the mass unbalances of the bare mesh (Figure 17 b).

a) b)

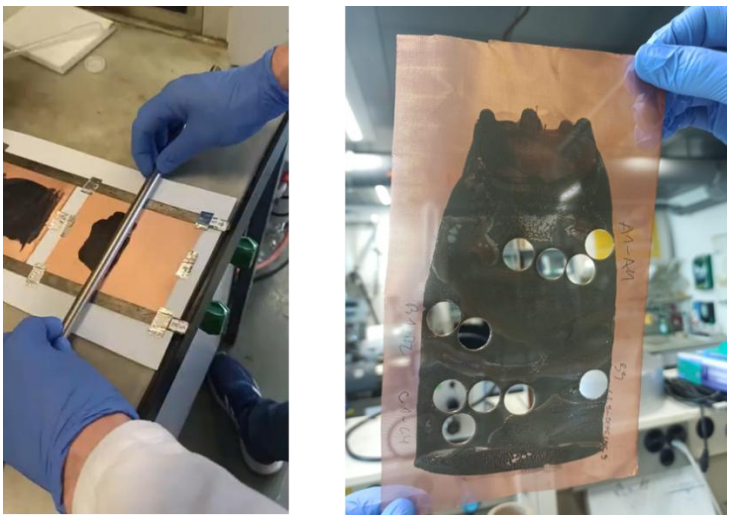

*Figure 17: a) Previously used bar coating method to obtain mesh electrodes; b) exemplary mesh electrode obtained from bar coating. Electrodes were punched in areas with seemingly homogeneous loading, which corresponds to only a small fraction of the total coating area.*

With the goal to obtain more reproducible, homogeneous coatings and a smaller mass error, it was therefore set as a target to use bladecoating instead, which allows to accurately control coating speed and the gap between the substrate and the blade, and which turned out to be an excellent choice for the manufacturing of LMFP mesh electrodes. Two meshes with a lower mass error compared to the original mesh (Figure 18 a) were identified and chosen as potential substrates for a bladecoating process. Next, the slurry composition was tuned to achieve all the goals listed in Figure 18 b. Figure 18 c shows pictures of the slurry manufacturing process and pictures of the final coating on steel mesh (Steel mesh 212/90 µm, Bopp AG, Switzerland).

All following OEMS tests were carried out with electrodes made using the described manufacturing method.



Funded by the European Union

a)

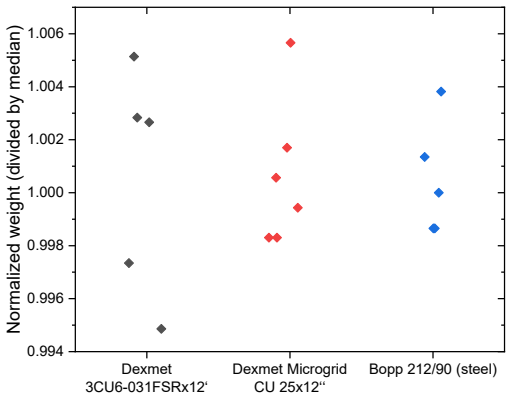


b)


c)

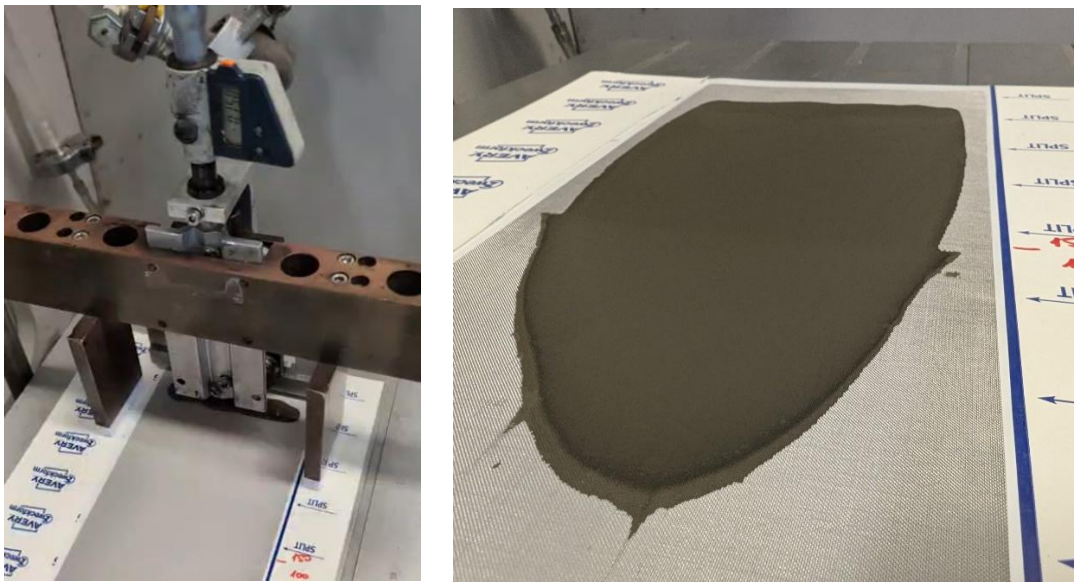

*Figure 18: a) Column scatter plots of circular blank mesh weights (13 mm diameter), divided by median; b) targets for a suitable slurry composition; c) blade coating process on Bopp steel mesh, attached to sticky underground and finished coating after slurry application.*

## 1.4.4 Conclusions

To summarize, this section describes:

- The isotope labelling strategy developed to attribute the source of gassing to single solvent components in a realistic electrolyte mixture
- OEMS tests of LMFP electrodes, with no gassing observed in the operational window
- Electrochemical cycling experiments of Silicon electrodes in different electrolytes
- Preliminary OEMS tests of Silicon electrodes, showing major differences in the $H_2$ evolution of half-cells and full-cells, and half-cells built with different binders. In contrast, CO, $CO_2$ and $C_2H_4$ evolution onset potentials are comparable
- A new electrode manufacturing approach for Silicon OEMS electrodes



Funded by the European Union

1. Strobl M, Baur ME, Samothrakitis S, et al. Concurrent Operando Neutron Imaging and Diffraction Analysis Revealing Spatial Lithiation Phase Evolution in an Ultra-Thick Graphite Electrode. *Adv Energy Mater*. 2025;15(20). doi:10.1002/aenm.202405238

2. Carreón Ruiz ER, Lee J, Márquez Damián JI, et al. Spectroscopic neutron imaging for resolving hydrogen dynamics changes in battery electrolytes. *Mater Today Adv*. 2023;19. doi:10.1016/j.mtadv.2023.100405

3. Ziesche RF, Kardjilov N, Kockelmann W, Brett DJL, Shearing PR. Neutron imaging of lithium batteries. *Joule*. 2022;6(1):35-52. doi:10.1016/j.joule.2021.12.007

4. Sears VF. Neutron scattering lengths and cross sections. *Neutron News*. 1992;3(3):26-37. doi:10.1080/10448639208218770

5. Boillat P, Trtik P, Lehmann EH, et al. Who made the noise? Systematic approach for the assessment of neutron imaging scintillators. *Opt Express*. 2024;32(8):14471. doi:10.1364/oe.511939

6. Winter E. Fundamental Understanding of Critical Parameters Enabling Lithium Metal Batteries. 2023;(29026). doi:10.3929/ethz-b-000592384

7. Losko AS, Han Y, Schillinger B, et al. New perspectives for neutron imaging through advanced event-mode data acquisition. *Sci Rep*. 2021;11(1):1-11. doi:10.1038/s41598-021-00822-5

8. Ziegler JF, Ziegler MD, Biersack JP. SRIM – The stopping and range of ions in matter (2010). *Nucl Instruments Methods Phys Res Sect B Beam Interact with Mater Atoms*. 2010;268(11-12):1818-1823. doi:10.1016/J.NIMB.2010.02.091

9. Lundström R, Gogoi N, Hou X, Berg EJ. Competing Ethylene Carbonate Reactions on Carbon Electrode in Li-Ion Batteries. *J Electrochem Soc*. 2023;170(4):040516. doi:10.1149/1945-7111/accb6e

10. Jeschull F, Zhang L, Kondracki Ł, Scott F, Trabesinger S. Interphase formation with carboxylic acids as slurry additives for Si electrodes in Li-ion batteries. Part 1: performance and gas evolution. *JPhys Energy*. 2023;5(2). doi:10.1088/2515-7655/acbbed

## 1.5 SIMS based operando methodology

SIMS is particularly promising as an analytical technique for batteries because of its capability of detecting Li, even at trace concentrations. Operando characterization techniques are particularly important in this regard, as they can provide direct insights into Li-ion kinetics by enabling real-time tracking of changes within a functioning battery. Therefore, operando SIMS methodologies offer valuable opportunities to advance the understanding of Li transport at electrode–electrolyte interfaces and related degradation processes. In this context, a few recent studies have employed SIMS analysis of solid-state batteries in their operational environment. Masuda et al. developed an in-situ ToF-SIMS based methodology for imaging Li distribution in composite cathode materials after charge/discharge[1]. They analyzed an all-solid-state battery with $LiCoPO_4$ (LCP) as the active material in cathode and $Li_{1+x}Al_xGe_{2-x}(PO_4)_3$ (LAGP) as a solid electrolyte and were able to image a cyclic increase-decrease of Li intensity in the LCP particles after each charge-discharge cycle. Yamagishi et al. also



Funded by the European Union

developed a similar ToF-SIMS based in-situ imaging technique[2]. More recently Cressa et al. reported a workflow that allowed them in-situ correlative SE-SIMS imaging at nanoscale lateral resolution of a LLZO based solid state battery before and after cell failure[3]. They mapped presence of Li on the new phases that appeared inside the LLZO after cell failure, confirming them to be the Li dendrites. Although these reported studies showed the possibility of performing electrochemical charging inside the SIMS instruments, one major limitation of these quasi-operando methods is that the electrochemical operation of the cell had to be stopped or paused during analysis. The electrochemical operation of a cell is inherently a non-equilibrium process, so, tracking the non-equilibrium changes in Li distribution in solid state batteries during electrochemical charging requires a fully operando SIMS technique that would allow us to perform SIMS analysis without interruption of the electrochemical processes in the battery.

In the following subsection, we present our prototyping efforts to address the instrumental challenges in the context of operando SIMS analysis. We describe the custom electrochemical cycling setup and sample holder designed to facilitate real time SIMS imaging of SSBs. Finally, to valorize our operando SIMS method, we present results from a proof-of-concept operando SIMS experiment, capturing in real-time the spatial Li redistribution in a gel polymer electrolyte solid-state battery during battery operation.

## 1.5.1 *Operando* setup development:

The prototype platform used for developing the operando workflow consists of a dual-beam FIB-SEM (Thermofisher Scientific) fitted with a double focusing compact magnetic sector mass spectrometer developed at LIST[4]. This specific platform utilizes the Ga-FIB as the primary ion beam and use of a continual focal plane detector allows detection of all masses in parallel. This FIB-SIMS system allows us to achieve sub-20nm lateral resolution for SIMS-based elemental mapping, paving the way for us to track nano-scale Li transport in batteries.

Performing SIMS analysis during electrochemical cycling is challenging because SIMS requires an extraction field between the sample surface and the SIMS optics for collection of secondary ions sputtered by the primary beam. In the FIB-SIMS system used here, this electric field is established by applying a ±500 V bias to the sample relative to the grounded first electrode of the SIMS optics[4]. This voltage bias makes it incompatible with conventional potentiostats for electrochemical cycling hindering operando SIMS analysis.

To overcome this limitation, an in-house special electrochemical cycling unit was developed. Our setup works by referencing the terminals of the potentiostat at 500 V, this serves two key purposes:

1. It maintains the necessary extraction field needed for secondary ion collection by elevating both battery electrodes to 500 V.
2. It allows us to conduct electrochemical cycling concurrently with SIMS analysis, using 500 V as the baseline potential to create a small potential difference between the electrodes to drive electrochemical reactions.

Furthermore, as no commercial sample holders are available for operando FIB-SIMS analysis a special holder was designed in-house with following considerations in mind:

-adaptability to the FIB-SIMS platform and inert gas transfer shuttle for contamination free transfer from glovebox to the analysis chamber.


Funded by the European Union
OPINCHARGE

-capability of applying dynamic stacking pressure to maintain intimate contact between the electrode and electrolyte to ensure reliable electrochemical performance.

-stable interface between the electrical contacts of the holder and the cycling unit for noise free electrochemical operation.

Figure 22 elucidates the schematic of the operando setup as well as the design of the sample holder and a real-time view from the analysis chamber during operando measurements

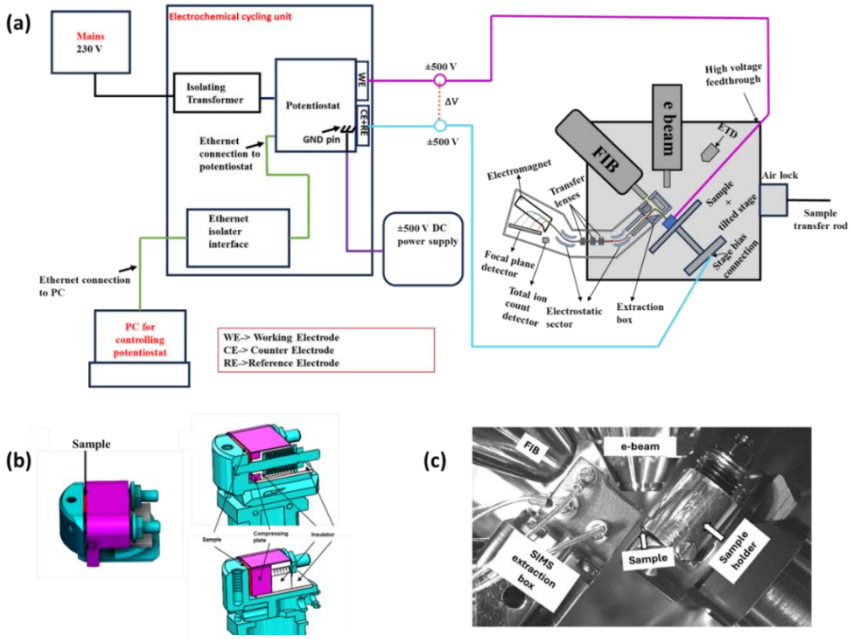


*Figure 19 (a) Schematic of the operando FIB-SIMS setup. (b) 3D design of the sample holder, the two electrical contacts are shown in different color. (C) in chamber view during operando analysis*

## 1.5.2 Proof-of-concept experiment: tracking Li-ion migration pathways in SSBs

As a proof-of-concept study, here we tracked Li transport in a gel polymer electrolyte-based Li symmetric cell[5].

### 1.5.2.1 Sample details

(i) Electrolyte: The electrolyte is a gel polymer electrolyte (referred hereafter as GPE) composed of a poly (vinylidene fluoride-co-hexafluoropropylene) (PVDF-HFP) polymer matrix. The matrix is plasticized with polyethylene glycol dimethyl ether (PEGDME, Mn = 500 g/mol) serving as the solvent, and lithium bis(trifluoromethanesulfonyl)imide (LiTFSI) as the lithium salt. The LiTFSI salt had natural Li abundance. Both the LiTFSI salt and the plasticizer used here for preparing the GPE were purchased from Sigma-Aldrich. The solvent-to-salt composition was adjusted to provide an ethylene oxide units to lithium cation (EO/Li) molar ratio of 20:1. The GPE was synthesized via the solvent casting method and exhibited an ionic conductivity of $3.4\times10^{-4}$ S cm$^{-1}$ at room temperature[6]. In comparison with conventional carbonate-based solvents (EC + EMC) used in liquid electrolytes, the GPE demonstrated markedly improved flame resistance, attributable to the low vapor pressure of the PEGDME solvent. These characteristics highlight its strong potential as a candidate for next-generation solid-state batteries.



Funded by the European Union
OPINCHARGE

(ii) Electrodes and isotope labelling: For *operando* analysis, Li foil was used as both the working electrode (W.E.) and counter electrode (C.E.). The W.E. of this symmetrical cell was enriched in $^{6}$Li. $^{6}$Li-chunks (enriched to 95.4 % in $^{6}$Li, immersed in mineral oil) were purchased from Sigma Aldrich (CAS- No. 14,258–72–1). The C.E. used here was a Li foil having Natural Li abundance, i.e., they were rich in $^{7}$Li (delivered by Alfa Aesar, CAS-No. 7439–93–2). First, an 8 mm-diameter semicircular disc of the GPE was prepared using a lithium disc punching tool and a scalpel. For the isotopically labeled W.E., $^{6}$Li metal chunks were washed with cyclohexane to remove residual mineral oil and subsequently roll-pressed by a rolling pin into foils of approximately 0.4 mm thickness. From one of these foils, a 6 mm-diameter circular disc was punched and then cut into a semicircular shape with a scalpel. The counter electrode was prepared in the same manner from lithium foil of natural isotopic abundance. The GPE was then placed between the two semicircular lithium foils and carefully mounted in the *operando* sample holder (described in previous section), ensuring that the flat side of the assembly was oriented toward the electron/ion beam for analysis. Stacking pressure was applied via the movable compression plate of the sample holder to ensure good interfacial contact between electrodes and the GPE. All preparation and cell assembly steps were conducted inside an argon-filled glovebox ($O_2$ < 1 ppm, $H_2O$ < 1 ppm) to prevent exposure to air and moisture. The sample was transferred from the glovebox to the FIB-SEM-SIMS platform using an inert gas transfer shuttle. The sample holder along with the sample is first loaded inside the shuttle in Ar atmosphere and the shuttle is sealed. After removal of the sealed shuttle from the glovebox, it is taken to the airlock of the FIB-SEM-instrument and is mounted on the airlock. The shuttle is opened once the airlock is purged with Ar, and the sample holder is transferred inside the analysis chamber through a valve connecting the airlock and the analysis chamber.

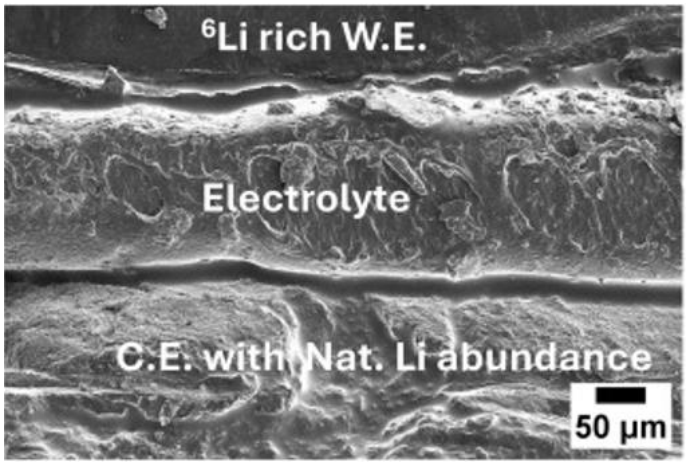


*Figure 20 SE image of the planar surface of the semi-circular cell assembly used for the operando SIMS imaging*

#### 1.5.2.2 Operando analysis

After transferring the sample from the glovebox to the FIB-SIMS chamber, SE images of the pristine electrolyte were collected at 5 keV and 50–100 pA (Figure 23). The stage was tilted to 52° for normal incidence of the FIB, and SIMS imaging was performed near the GPE-W.E. interface to assess the initial $^{6}$Li distribution.

Electrochemical cycling was carried out using a chronopotentiometry (CP) sequence at 100 µA/cm² for 200 min, corresponding to the theoretical consumption of ~1.6 µm of the $^{6}$Li-rich foil. Voltage response was recorded, and SE and SIMS images were acquired at the GPE/W.E. interface at selected


Funded by the European Union
OPINCHARGE

time points. Data were processed using Python and Fiji to generate $^{6}Li/(^{6}Li+^{7}Li)$ ratio maps, providing a semi-quantitative measure of ionic transport relative to the pristine state.

#### 1.5.2.3 Results and discussion

Figure 24(a) shows the voltage profile recorded during the CP sequence, the red circles mark the specific time points at which SIMS imaging was carried out. Figure 24(b) displays the spatially resolved $^{6}Li/ (^{6}Li + ^{7}Li)$ ratio maps obtained from a selected region of the GPE located near its interface with the W.E. during the CP sequence. These two-dimensional maps reveal a distinct and progressive enrichment of $^{6}Li$ in the investigated ROI during the electrochemical charging process. Clearly demonstrate that the concentration of $^{6}Li$ in the electrolyte increased steadily throughout the operando experiment. This increase in $^{6}Li$ content can be understood by considering the ion-exchange dynamics occurring during charging. The GPE was prepared using non-isotopically labeled LiTFSI salt, meaning that its lithium reservoir predominantly consisted of $^{7}Li$. During the charging sequence, part of the $^{7}Li$ originally present in the GPE migrated toward the C.E. and was plated as $Li^{0}$. At the same time, in order to maintain charge neutrality in the system, $^{6}Li$ ions from the W.E. migrated into the GPE, and replaced the depleted $^{7}Li$ population. This process accounts for the observed increase in the $^{6}Li$ fraction within the GPE as electrochemical charging progresses. These results validate the applicability of our setup for localized high-resolution visualization of the transient changes in lithium-ion distribution inside a battery during operation.

From the SIMS ratio maps it is clear that the $^{6}Li$ enrichment during the CP sequence occurred heterogeneously. These heterogenous $^{6}Li$ enrichment was further confirmed from the data of separately run operando experiments (not shown here). A number of reasons are attributable to this observed heterogeneity:

-The plating/stripping of Li from the W.E. and C.E. respectively might be uneven due to initial roughness of the electrode surface and the corresponding non-uniform contact between the electrode and the electrolyte. This non-uniform contact will lead to localized electric field gradients and inhomogeneous $^{6}Li$ flux.

- The other reason could be the fact that the ion transport pathway in the GPE depends on its crystallinity. As discussed in literature regarding the ion transport mechanism in gel polymer electrolytes, the ion percolation network forms through the liquid-rich amorphous regions of the electrolyte[7], which fits with the observed heterogenous enrichment of $^{6}Li$ in Figure 24(b).

Another notable observation from SIMS maps is that the $^{6}Li$ fraction in the electrolyte, measured prior to electrochemical charging, exceeds the natural abundance of $^{6}Li$. Reference measurements with Li metal samples for the same SIMS imaging parameters suggest that the observed increase is not due to detector saturation. The sample had been left overnight in the FIB-SEM-SIMS instrument after assembly before any SIMS measurements were conducted, allowing spontaneous diffusion of $^{6}Li$ ions from the electrode into the electrolyte due to the chemical concentration gradient.


Funded by the European Union

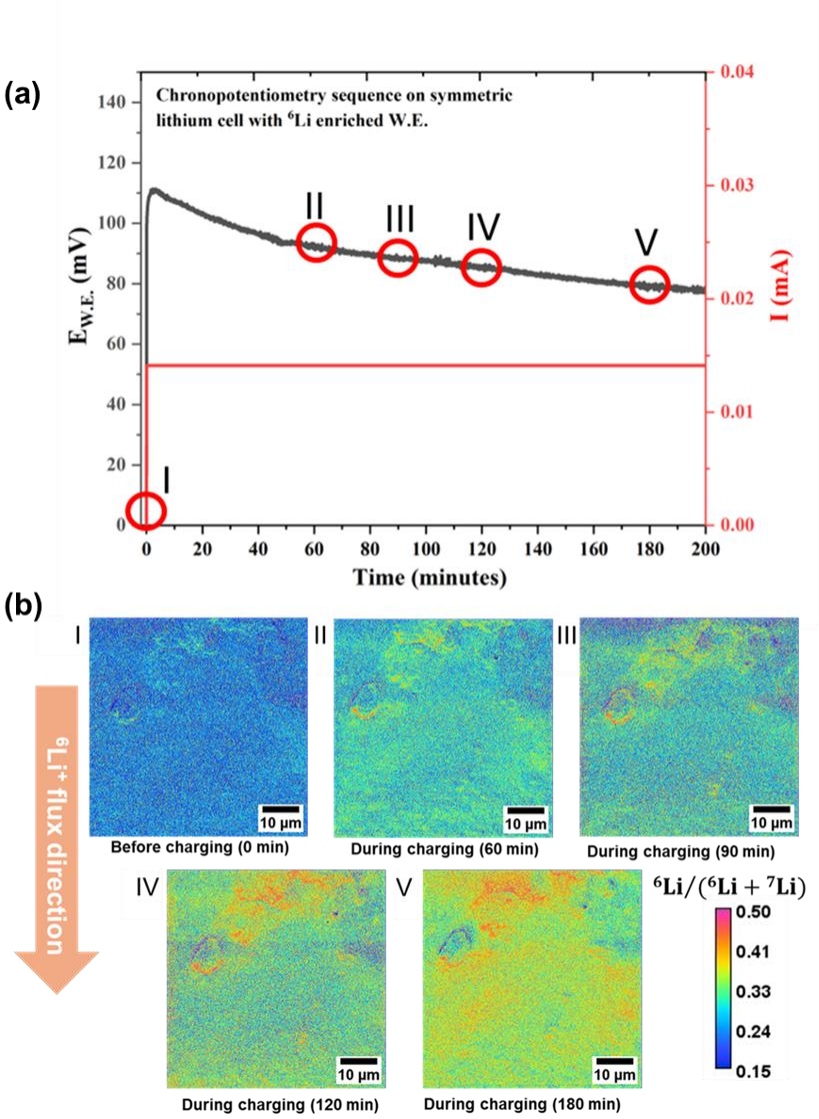


*Figure 21 (a) Voltage profile recorded during the operando experiment. A constant current of current density 100 µA/cm² was applied. The red circles are representative of the time points at which operando imaging was done. (b) Time series of 2D $^{6}Li/(^{6}Li+^{7}Li)$ ratio maps from the same ROI before and during electrochemical charging (Field of View (FOV)=59 µm x 59 µm, 512 × 512 pixels, Primary beam energy=30 keV, primary beam current=50 pA, dwell time per pixel=0.5 ms). The color bar represents different values of $^{6}Li$ fraction. The top side of each SIMS ratio map corresponds to the region near the $^{6}Li$ enriched W.E., and the arrow indicates the direction of the incoming $^{6}Li$ ionic flux.*

This process led to the elevated $^{6}Li$ fraction even in the absence of an applied current. Spontaneous diffusion of lithium ions without external bias has been reported previously in both liquid and solid electrolytes. Because this phenomenon can occur concurrently with external electrical current-driven electro-migration of Li-ions during charging, it is essential to distinguish the contribution of spontaneous diffusion from that of the applied current when interpreting the operando results. From the results of a control experiment for same time as the CP sequence applied during the operando experiment, it was concluded that at room temperature spontaneous diffusion of Li (due to chemical concentration gradient) detected by SIMS imaging is negligible compared to the observed Li electromigration reported here.


Funded by the European Union
OPINCHARGE

## 1.5.3 Conclusions

To summarize this section describes:

- Development of a new operando FIB-SIMS imaging workflow allowing simultaneous SIMS analysis and electrochemical operation of sold-state batteries.
- Li isotope tracing here allowed us to track the Li electromigration through a gel polymer electrolyte
- Observed heterogenous enrichment of $^{6}Li$ in the electrolyte agrees with the ion percolation mechanism through gel polymer electrolytes elucidated in literature[7].
- The methodology can be extended to understand ion transport in composite electrode/electrolytes as well as the SEI layers of SSBs
- To best of our knowledge, the setup described here is first to facilitate correlative analysis combining SE, BSE and SIMS information in operando condition. This paves the way for deeper insights into link between microstructural and chemical degradations processes in Li-ion batteries and their effect on electrochemical performance.

# 1.6 References


1. Masuda H, Ishida N, Ogata Y, Ito D, Fujita D. In situ visualization of Li concentration in all-solid-state lithium ion batteries using time-of-flight secondary ion mass spectrometry. J Power Sources. 2018;400:527-532. doi:10.1016/j.jpowsour.2018.08.040

2. Yamagishi Y, Morita H, Nomura Y, Igaki E. Visualizing Lithiation of Graphite Composite Anodes in All-Solid-State Batteries Using Operando Time-of-Flight Secondary Ion Mass Spectrometry. Journal of Physical Chemistry Letters. 2021;12(19):4623-4627. doi:10.1021/acs.jpclett.1c01089

3. Cressa L, Sun Y, Andersen D, et al. Toward Operando Structural, Chemical, and Electrochemical Analyses of Solid-State Batteries Using Correlative Secondary Ion Mass Spectrometry Imaging. Anal Chem. 2023;95(26):9932-9939. doi:10.1021/acs.analchem.3c01059

4. De Castro O, Audinot JN, Hoang HQ, et al. Magnetic Sector Secondary Ion Mass Spectrometry on FIB-SEM Instruments for Nanoscale Chemical Imaging. Anal Chem. 2022;94(30):10754-10763. doi:10.1021/acs.analchem.2c01410

5. Sharma S, Santiago A, Martinez-Ibañez M, et al. Operando visualization of Li distribution in solid-state batteries using focused ion beam-secondary ion mass spectrometry imaging. Electrochim Acta. 2025;536:146728. doi:10.1016/j.electacta.2025.146728

6. Castillo J, Santiago A, Judez X, et al. Safe, Flexible, and High-Performing Gel-Polymer Electrolyte for Rechargeable Lithium Metal Batteries. Chemistry of Materials. 2021;33(22):8812-8821. doi:10.1021/acs.chemmater.1c02952

7. Patel M, Chandrappa KG, Bhattacharyya AJ. Increasing ionic conductivity of polymer–sodium salt complex by addition of a non-ionic plastic crystal. Solid State Ion. 2010;181(17-18):844-848. doi:10.1016/j.ssi.2010.04.013